Atmos. Chem. Phys., 20, 9183–9207, 2020
https://doi.org/10.5194/acp-20-9183-2020
© Author(s) 2020. This work is distributed under
the Creative Commons Attribution 4.0 License.

Atmospheric Chemistry and Physics
Open Access
EGU

Molecular understanding of new-particle formation from α-pinene between -50 and $+25\,^{\circ}C$

Mario Simon[1], Lubna Dada[2], Martin Heinritzi[1], Wiebke Scholz[3,4], Dominik Stolzenburg[5], Lukas Fischer[3], Andrea C. Wagner[1,6], Andreas Kürten[1], Birte Rörup[2], Xu-Cheng He[2], João Almeida[7,8], Rima Baalbaki[2], Andrea Baccarini[9], Paulus S. Bauer[5], Lisa Beck[2], Anton Bergen[1], Federico Bianchi[2], Steffen Bräkling[10], Sophia Brilke[5], Lucia Caudillo[1], Dexian Chen[11], Biwu Chu[2], António Dias[7,8], Danielle C. Draper[12], Jonathan Duplissy[2,13], Imad El-Haddad[9], Henning Finkenzeller[6], Carla Frege[9], Loic Gonzalez-Carracedo[5], Hamish Gordon[11,13], Manuel Granzin[1], Jani Hakala[2], Victoria Hofbauer[11], Christopher R. Hoyle[9,15], Changhyuk Kim[16,17], Weimeng Kong[17], Houssni Lamkaddam[9], Chuan P. Lee[9], Katrianne Lehtipalo[2,18], Markus Leiminger[3,4], Huajun Mai[17], Hanna E. Manninen[7], Guillaume Marie[1], Ruby Marten[9], Bernhard Mentler[3], Ugo Molteni[9], Leonid Nichman[19,a], Wei Nie[20], Andrea Ojdanic[5], Antti Onnela[7], Eva Partoll[3], Tuukka Petäjä[2], Joschka Pfeifer[1,7], Maxim Philippov[21], Lauriane L. J. Quéléver[2], Ananth Ranjithkumar[14], Matti P. Rissanen[2,22], Simon Schallhart[2,18], Siegfried Schobesberger[23], Simone Schuchmann[7], Jiali Shen[2], Mikko Sipilä[2], Gerhard Steiner[3,b], Yuri Stozhkov[21], Christian Tauber[5], Yee J. Tham[2], António R. Tomé[24], Miguel Vazquez-Pufleau[5], Alexander L. Vogel[1,7], Robert Wagner[2], Mingyi Wang[11], Dongyu S. Wang[9], Yonghong Wang[2], Stefan K. Weber[7], Yusheng Wu[2], Mao Xiao[7], Chao Yan[2], Penglin Ye[11,25], Qing Ye[11], Marcel Zauner-Wieczorek[1], Xueqin Zhou[1,9], Urs Baltensperger[9], Josef Dommen[9], Richard C. Flagan[17], Armin Hansel[3,4], Markku Kulmala[2,13,20,26], Rainer Volkamer[6], Paul M. Winkler[5], Douglas R. Worsnop[2,10,25], Neil M. Donahue[11], Jasper Kirkby[1,7], and Joachim Curtius[1]

[1]Institute for Atmospheric and Environmental Sciences, Goethe University Frankfurt, 60438 Frankfurt am Main, Germany
[2]Institute for Atmospheric and Earth System Research, University of Helsinki, Helsinki, 00014, Finland
[3]Institute for Ion Physics and Applied Physics, University of Innsbruck, Innsbruck, 6020, Austria
[4]Ionicon Analytik GmbH, Innsbruck, 6020, Austria
[5]Faculty of Physics, University of Vienna, Vienna, 1090, Austria
[6]Department of Chemistry & CIRES, University of Colorado Boulder, Boulder, CO 80309-0215, USA
[7]CERN, Geneva, 1211, Switzerland
[8]Faculdade de Ciências, Universidade de Lisboa, Lisbon, 1749-016, Portugal
[9]Laboratory of Atmospheric Chemistry, Paul Scherrer Institute, PSI, Villigen, 5232, Switzerland
[10]TOFWERK AG, Thun, 3600, Switzerland
[11]Center for Atmospheric Particle Studies, Carnegie Mellon University, 5000 Forbes Avenue, Pittsburgh, PA 15213, USA
[12]Department of Chemistry, University of California, Irvine, CA 92697, USA
[13]Helsinki Institute of Physics, University of Helsinki, Helsinki, 00014, Finland
[14]School of Earth and Environment, University of Leeds, Leeds, LS2 9JT, UK
[15]Institute for Atmospheric and Climate Science, Swiss Federal Institute of Technology, Zurich, 8092, Switzerland
[16]School of Civil and Environmental Engineering, Pusan National University, Busan, 46241, Republic of Korea
[17]Division of Chemistry and Chemical Engineering, California Institute of Technology, Pasadena, CA 91125, USA
[18]Finnish Meteorological Institute, Helsinki, 00560, Finland
[19]Department of Earth and Environmental Sciences, University of Manchester, Manchester, M13 9PL, UK
[20]Joint International Research Laboratory of Atmospheric and Earth System Sciences, School of Atmospheric Sciences, Nanjing University, Nanjing, Jiangsu Province, China
[21]P. N. Lebedev Physical Institute of the Russian Academy of Sciences, Moscow, 119991, Russia
[22]Aerosol Physics Laboratory, Physics Unit, Faculty of Engineering and Natural Sciences, Tampere University, 33101 Tampere, Finland
[23]Department of Applied Physics, University of Eastern Finland, Kuopio, 70211, Finland

Published by Copernicus Publications on behalf of the European Geosciences Union.

[24]IDL, Universidade da Beira Interior, R. Marquês de Ávila e Bolama, Covilhã, 6201-001, Portugal
[25]Aerodyne Research Inc., Billerica, MA 01821, USA
[26]Aerosol and Haze Laboratory, Beijing Advanced Innovation Center for Soft Matter Science and Engineering, Beijing University of Chemical Technology, Beijing, China
[a]present address: Aerospace Research Centre, National Research Council of Canada, Ottawa, ON, K1V 9B4, Canada
[b]present address: Grimm Aerosol Technik Ainring GmbH & Co KG, 83404 Ainring, Germany

Correspondence: Mario Simon (simon@iau.uni-frankfurt.de) and Joachim Curtius (curtius@iau.uni-frankfurt.de)

Received: 15 November 2019 – Discussion started: 21 January 2020
Revised: 27 May 2020 – Accepted: 19 June 2020 – Published: 3 August 2020

Abstract. Highly oxygenated organic molecules (HOMs) contribute substantially to the formation and growth of atmospheric aerosol particles, which affect air quality, human health and Earth's climate. HOMs are formed by rapid, gas-phase autoxidation of volatile organic compounds (VOCs) such as α-pinene, the most abundant monoterpene in the atmosphere. Due to their abundance and low volatility, HOMs can play an important role in new-particle formation (NPF) and the early growth of atmospheric aerosols, even without any further assistance of other low-volatility compounds such as sulfuric acid. Both the autoxidation reaction forming HOMs and their NPF rates are expected to be strongly dependent on temperature. However, experimental data on both effects are limited. Dedicated experiments were performed at the CLOUD (Cosmics Leaving OUtdoor Droplets) chamber at CERN to address this question. In this study, we show that a decrease in temperature (from $+25$ to -50 °C) results in a reduced HOM yield and reduced oxidation state of the products, whereas the NPF rates ($J_{1.7\,\mathrm{nm}}$) increase substantially. Measurements with two different chemical ionization mass spectrometers (using nitrate and protonated water as reagent ion, respectively) provide the molecular composition of the gaseous oxidation products, and a two-dimensional volatility basis set (2D VBS) model provides their volatility distribution. The HOM yield decreases with temperature from 6.2 % at 25 °C to 0.7 % at -50 °C. However, there is a strong reduction of the saturation vapor pressure of each oxidation state as the temperature is reduced. Overall, the reduction in volatility with temperature leads to an increase in the nucleation rates by up to 3 orders of magnitude at -50 °C compared with 25 °C. In addition, the enhancement of the nucleation rates by ions decreases with decreasing temperature, since the neutral molecular clusters have increased stability against evaporation. The resulting data quantify how the interplay between the temperature-dependent oxidation pathways and the associated vapor pressures affect biogenic NPF at the molecular level. Our measurements, therefore, improve our understanding of pure biogenic NPF for a wide range of tropospheric temperatures and precursor concentrations.

1 Introduction

Atmospheric aerosol particles play a key role in the regulation of climate by influencing Earth's radiative energy balance (IPCC, 2013). In order to affect the solar radiation budget by acting as cloud condensation nuclei (CCN), newly formed particles have to reach a size of 50 to 100 nm (Dusek et al., 2006); i.e., they need to grow fast enough to avoid coagulation scavenging by preexisting particles. Furthermore, fine airborne particles affect the air quality, are responsible for most air-pollution-related diseases and cause millions of premature deaths worldwide (WHO, 2016).

Around half of the global CCN originate from nucleation of organic or inorganic atmospheric vapors (Spracklen et al., 2008; Merikanto et al., 2009; Kulmala et al., 2013; Gordon et al., 2017). New-particle formation (NPF) is observed in many environments and under various conditions around the globe, from remote locations such as forested areas or marine and coastal regions to polluted urban areas; from warm environments, such as the tropics, to cold polar and alpine regions; and from Earth's surface to the free troposphere (Kulmala et al., 2004; Kerminen et al., 2018). Gaseous sulfuric acid (Ball et al., 1999; Kuang et al., 2008), ammonia (Kirkby et al., 2011; Kürten et al., 2016), amines (Kurtén et al., 2008; Almeida et al., 2013; Kürten et al., 2014), iodine (O'Dowd et al., 2002; Sipilä et al., 2016) and biogenic volatile organic compounds (BVOCs; Donahue et al., 2013; Riccobono et al., 2014; Kirkby et al., 2016; Bianchi et al., 2016) have been identified as key vapors involved in atmospheric NPF. The relative importance of each these precursors, however, depends on the particular ambient conditions. The chemical composition of the newly formed particles is also widely influenced by volatile organic compounds (VOCs), which undergo atmospheric reactions to form secondary organic aerosols (SOAs; Jimenez et al., 2009; Hallquist et al., 2009; Riipinen et al., 2012).

BVOCs emitted by vegetation comprise the dominant fraction of all VOCs, with an estimated global emission rate of 760 TgC per year. Monoterpenes contribute approximately 11 % of all BVOC emissions (Sindelarova et al., 2014). The dominant monoterpene from vegetation (e.g., conifer-

ous trees) is α-pinene, accounting for $\sim 34\,\%$ of the total global monoterpene emissions. Most of its oxidation products lead to oxidized volatile organic compounds (OVOCs) with a low degree of oxygenation; they are characterized as intermediate-volatility or semivolatile organic compounds (IVOCs, $300 < C^*(T) < 3\times10^6\,\mu g\,m^{-3}$, and SVOCs, $0.3 < C^*(T) < 300\,\mu g\,m^{-3}$, respectively, where $C^*(T)$ is the effective saturation concentration). However, α-pinene has an endocyclic carbon double bond; oxidation of this functionality by ozone can initiate a rapid oxidation process, known as autoxidation (Crounse et al., 2013). Autoxidation proceeds by repeated intramolecular hydrogen shifts (H shifts) of weakly bound hydrogen atoms within peroxy radicals ($RO_2^\bullet$). Each H shift is followed by the rapid addition of molecular oxygen (O_2) to form multifunctional peroxy radicals with a high degree of oxygenation, while preserving the radical functionality. Under low-NO conditions (Berndt et al., 2018a), these radicals terminate into organic products with a high degree of oxygenation and therefore low volatility. Although multifunctional $RO_2^\bullet$ radicals formed in the autoxidation process represent an important intermediate class of compounds in atmospheric chemistry (Rissanen et al., 2015), knowledge about their complex formation mechanisms and kinetics remains far from complete (Ehn et al., 2017).

The autoxidation pathway leads to highly oxygenated organic molecules (HOMs) with molar yields of several percent (7 % at 20 °C, Ehn et al., 2014; 3.2 % at 5 °C, Kirkby et al., 2016). This class of oxidation products spans a wide range of volatilities from low-volatility and extremely low volatility towards ultralow-volatility organic compounds (LVOCs, $3\times10^{-5} < C^*(T) < 0.3\,\mu g\,m^{-3}$; ELVOCs, $3\times10^{-9} < C^*(T) < 3\times10^{-5}\,\mu g\,m^{-3}$; and ULVOCs, $C^*(T) < 3\times10^{-9}\,\mu g\,m^{-3}$, respectively). While the LVOC and ELVOC classes mainly contribute to the growth of embryonic clusters in the atmosphere, the new class ULVOC refers to molecules with sufficiently low saturation vapor pressure to enable them to reach supersaturation and drive pure biogenic nucleation (Donahue et al., 2012; Bianchi et al., 2019; Schervish and Donahue, 2020).

The fate of the α-pinene peroxy radicals (e.g., $C_{10}H_{15}O_{4,6,8,10}$) is mainly influenced by the presence of nitrogen oxides (NO_x), hydroxyl radicals ($HO_x^\bullet$) or peroxy radicals ($RO_2^\bullet$). Rapid bimolecular reactions terminate the autoxidation chain by forming closed-shell products and consequently affect the chemical composition of the oxidation products and the molar yield of HOMs (Presto et al., 2005; Ng et al., 2007; Ehn et al., 2014; Berndt et al., 2015; Rissanen, 2018). The reactions with NO and $HO_x^\bullet$ mainly form semivolatile and low-volatility organic compounds, which are important for the growth of particles with sizes above a few nanometers (Donahue et al., 2013; Wildt et al., 2014). Since NO concentrations are usually low in areas where BVOC emissions predominate, the loss of $RO_2^\bullet$ radicals in bimolecular reactions with NO can generally be neglected. In contrast, the $RO_2^\bullet$ cross-reaction can form higher-molecular-weight accretion products (ROOR; Donahue et al., 2011; Berndt et al., 2018b; Valiev et al., 2019). As shown by Tröstl et al. (2016) and Lehtipalo et al. (2018), these gaseous dimeric compounds have the ability to condense irreversibly onto atmospheric particles or even to contribute to the early-stage growth of molecular clusters, since they cover a wide range of volatility from low to ultralow vapor pressure. Furthermore, they are also potentially important for NPF, especially in environments dominated by biogenic precursors, e.g., boreal forests (Mohr et al., 2017; Bianchi et al., 2017).

The bimolecular termination reactions have little or no energy barrier. Their rates are therefore only weakly affected by temperature. In contrast, quantum chemical calculations suggest that the intramolecular isomerization through H shifts within the peroxy radicals has a high activation barrier of $84\,kJ\,mol^{-1}$ or more (Rissanen et al., 2014; Kurtén et al., 2015; Schervish and Donahue, 2020). This results in a strong temperature dependence of the autoxidation, which slows down the oxygenation (HOM yield) at lower temperatures. Consequently, the chemical composition of the initial clusters formed from monoterpene oxidation changes at colder temperatures. This was shown in Frege et al. (2018) for ion-induced nucleation of pure HOM particles. Further, chamber studies showed that not only does the SOA formation rate of monoterpene oxidation have a strong temperature dependence, but also the final HOM distribution is affected by the autoxidation rate (Saathoff et al., 2009; Kristensen et al., 2017; Quéléver et al., 2019). Additionally, a recent model study by Schervish and Donahue (2020) showed that the first H-shift reaction of the peroxy radical isomerization is the rate-limiting step of total HOM formation. Stolzenburg et al. (2018) showed that, despite the reduction in HOM yield, there was no effect on the growth rate of new particles at lower temperatures. It was shown that the steep exponential temperature dependence in the saturation vapor pressure, as described by the Clausius–Clapeyron relation, counters the reduction in the oxidation state in terms of their volatility distribution. Recent measurements of particle composition by Ye et al. (2019) showed that this leads to sufficient condensation of even the low-oxygenated and moderately oxygenated organic products at low temperatures. The volatility of the oxidation products is relevant in order to characterize their ability to condense and participate in NPF. The volatility basis set (VBS) model is therefore a suitable tool to track the volatility change in the oxidation of volatile organic compounds with temperature.

Model simulations suggest that highly oxygenated organic molecules have a pronounced effect on NPF on a global scale, especially in pristine environments dominated by biogenic precursors such as the tropical rain forests or at high altitudes as well as in the preindustrial atmosphere (Gordon et al., 2017). Furthermore, recent observations support this conclusion, suggesting that oxidation products of BVOCs have a

major impact on the formation of CCN, especially at high altitudes in the tropical convective regions (Williamson et al., 2019). However, the lack of knowledge about the mechanisms and the accurate representation of NPF from BVOCs for different environmental conditions, especially their temperature dependence, remains a great challenge for atmospheric chemistry and climate models.

In the current study, we present a comprehensive investigation of the effect of ambient tropospheric temperature on the molecular composition of α-pinene oxidation products and NPF rates. The experiments were conducted at the CLOUD (Cosmics Leaving OUtdoor Droplets) chamber at CERN (Geneva, Switzerland), using atmospherically relevant concentrations of α-pinene and ozone. To study pure biogenic nucleation, the addition of other trace gases was avoided in this study. Going beyond the results of Stolzenburg et al. (2018), this study focuses on NPF over a wide range of tropospheric temperatures from ground level (25 °C) to the upper free troposphere (−50 °C).

2 Methods

2.1 The CLOUD experiment

The CERN CLOUD chamber is a 26.1 m^3 electropolished stainless-steel vessel for the study of NPF under atmospherically relevant conditions. The use of boiled-off nitrogen and oxygen from ultraclean cryogenic liquids in a ratio of 79 : 21 minimizes the levels of contaminants (e.g., SO_2, NH_3, NO_x or volatile organics) inside the chamber. CLOUD is operated at a slight overpressure (5 hPa) to avoid contamination at any time, especially when instruments are being connected or disconnected. The relative humidity is adjusted with a temperature-controlled Nafion humidifier using ultrapure Millipore water. Ozone and other trace gases are introduced by individual gas lines; gas dilution stages are applied when necessary to achieve the targeted mixing ratios.

To add monoterpene, dry nitrogen is passed through a temperature-controlled evaporator containing liquid α-pinene (Sigma-Aldrich, 98 %). Efficient uniform mixing of the gases and ions in the chamber is ensured by two magnetically coupled fans located at the bottom and top of the vessel. The characteristic wall loss rates of condensable gases can be adjusted by variation in the fan speed.

The ion concentration in the chamber can be regulated to values that are representative of the full range of tropospheric and stratospheric conditions by the controlled irradiation with a 3.5 GeV c^{-1} secondary π^+ beam from the CERN Proton Synchrotron. This simulates the ionizing muon irradiation in the upper troposphere and stratosphere. Furthermore, as the chamber is continuously exposed to galactic cosmic rays (GCRs), a 20 kV m^{-1} electrical high-voltage clearing field (HVCF) can be imposed by energizing two electrode grids located at the top and bottom of the chamber, removing all ions within seconds. Thus, the CLOUD chamber enables investigation of NPF under ion-free conditions as well as of ion concentrations that are found throughout the troposphere.

Photochemical processes, such as the photodissociation of ozone to produce $OH^\bullet$ radicals, can be controlled by homogeneous illumination with UV light of adjustable intensity. The light from four 200 W Hg–Xe UV lamps (UVH LC8, Hamamatsu Photonics K.K., Japan) is guided by a fiber-optic system into the chamber to avoid any heat load from the light sources and to establish near-homogenous illumination (Kupc et al., 2011).

A thermal housing surrounds the chamber to maintain a high temperature uniformity and to control the chamber temperature in a range from −70 to 100 °C with a precision of ±0.1 K. This stability is mandatory as many of the NPF and oxidation processes are highly sensitive to temperature. The temperature inside the chamber is measured with several arrays of thermocouples, while the chamber wall temperature is monitored by a set of calibrated Pt100 sensors (Dias et al., 2017).

Similar to previous CLOUD experiments, state-of-the-art instruments are used to determine the chamber conditions, the concentration of important gas species, and aerosol properties during nucleation and early-growth studies (Kirkby et al., 2016; Lehtipalo et al., 2018; Stolzenburg et al., 2018). All key instruments are placed in the midplane of the chamber to ensure sampling from well-mixed conditions inside the chamber. The sampling lines protrude 40 cm into the chamber to avoid sampling close to the walls and to reduce memory effects. Prior to changing to a new chemical system, the chamber and the sampling lines are rinsed with ultrapure water and subsequently heated up to 100 °C to clean the chamber from residual chemicals of previous experiments. Applying high ozone concentrations for several hours during the cleaning helps achieve contamination levels that are below parts per trillion by volume of inorganic and $< 150\,ppt_v$ of total organic compounds (Schnitzhofer et al., 2014). More details about the CLOUD experiment can be found in Kirkby et al. (2011) and Duplissy et al. (2016).

The experiments reported here were performed during the CLOUD10 (fall 2015), CLOUD12 (fall 2017) and CLOUD13 (fall 2018) campaigns. Within these three campaigns, sets of experiments at five different temperatures were performed to study the HOM production and NPF from α-pinene oxidation. α-Pinene was added to the chamber at volume mixing ratios ranging from 100 to 2000 ppt_v, while ozone levels were kept between 30 and 40 ppb_v. $OH^\bullet$ radicals were mainly formed by the ozonolysis of α-pinene with an 80 % yield (Chew and Atkinson, 1996) and also by UV photolysis of ozone. The relative humidity was commonly held at 40 % in CLOUD10 and CLOUD12 and 80 % in CLOUD13.

Before starting a NPF sequence (run), the CLOUD chamber was cleaned from residual particles and organic compounds by flushing the chamber with clean synthetic air for

several hours while operating the mixing fans at a high speed and periodically activating the HVCF to remove all charged aerosol particles efficiently. The results reported here were obtained without any addition of SO_2, NO_x or other trace gases in order to achieve a pure biogenic system, to isolate the chemistry of biogenic precursors and to avoid the interference with other potentially nucleating compounds. Furthermore, no $OH^{\bullet}$ radical scavenger was used during the experiments to ensure a faithful simulation of atmospheric conditions. The instruments and methods relevant for the present study are described in the following sections.

2.2 Nitrate CI-APi-TOF

The nitrate chemical ionization–atmospheric-pressure interface–time-of-flight mass spectrometer (CI-APi-TOF) uses nitrate anions ($(HNO_3)_n(NO_3^-)$, with $n = 0$–2) as reagent ions which are produced by exposing a sheath gas enriched by nitric acid (HNO_3) flow to a corona discharge (Kürten et al., 2011). Based on the free-jet-flow design of Eisele and Tanner (1993) the nitrate reagent ions are electrostatically pushed into the sample flow in the center of the ion–molecule-reaction drift region without mixing of both gas streams. After a reaction time of ~ 50 ms within the sample flow, the ions and charged clusters enter the atmospheric pressure interface of the mass spectrometer (APi-TOF, Tofwerk AG, Switzerland) where they are focused by two segmented quadrupole units and an ion lens assembly, while the pressure is gradually reduced to around 10^{-6} mbar. In the time-of-flight region, the ions are separated according to their mass-to-charge ratio and counted by a microchannel plate detector. The data are processed and analyzed in IGOR Pro (WaveMetrics, Inc., USA) using the software package Tofware (Version 3.1, Aerodyne Inc., USA).

The chemical ionization with nitrate anions is selective not only towards strong Lewis acids, like sulfuric acid (H_2SO_4; Jokinen et al., 2012) or iodic acid (HIO_3; Sipilä et al., 2016), but also for bases, like dimethylamine ($(CH_3)_2NH$) when ion clusters are being formed, including the nitrate reagent ions (Simon et al., 2016). Highly polar functional groups, like carboxylic acids (COOH), hydroperoxides (R-O-OH) and peroxy acids (R(O)-O-OH), which are the most abundant functional groups in HOMs, can also be detected (Hyttinen et al., 2015). While strong acids are mostly detected as deprotonated anions (e.g., HSO_4^-), HOMs are charged mainly through adduct-ion formation ($HOM_i \cdot NO_3^-$). Here, the index i denotes a specific HOM (with a specific exact mass). The concentration of the sample is achieved by normalization of the product ion count rates per second (cps) with the intensity of the reagent ions (cps) expressed by the following Eq. (1):

$$[HOM_i] = C \cdot TE_i \cdot SL_{HOM_i} \cdot \ln\left(1 + \frac{[HOM_i \cdot NO_3^-]}{\sum_{j=0}^{2}[(HNO_3)_j \cdot NO_3^-]}\right). \quad (1)$$

Three different correction factors are considered to obtain a concentration from the raw count rate. First, a general calibration coefficient, C, of the mass spectrometer is applied, which is determined from a calibration using sulfuric acid as described in Kürten et al. (2012). Here, we assume that all HOMs with an oxygen-to-carbon (O/C) ratio of ≥ 0.6 have a collision-limited charging efficiency when reacting with the nitrate ions similarly to sulfuric acid. In addition, we assume that the charging efficiency of the nitrate CI-APi-TOF technique does not change significantly with temperature or humidity (Viggiano et al., 1997). The estimated detection limit of the instrument for sulfuric acid is about 5×10^4 molec. cm^{-3}; however, due to a better signal-to-noise ratio at higher mass-to-charge ratios, some HOM_i can even be quantified at lower concentrations. Second, the mass-dependent transmission efficiency TE_i of the instrument is considered by depleting the reagent ions by various perfluorinated acids according to the method described by Heinritzi et al. (2016) in a separate characterization experiment at the beginning and end of the campaign. Third, a temperature-dependent sampling-line loss correction factor, SL_{HOM_i}, is considered. It depends on the sample flow rate, the diffusion coefficient of the target molecule and the length of the sampling line. We assume laminar flow diffusional loss in the 120 cm sampling line. To reduce wall losses we applied a core-sampling technique as described by Knopf et al. (2015) and Fu et al. (2019). A fraction of 8.5 standard liters per minute (slm) of the total flow in the inlet line (40 slm) is sampled from its center. This setup minimizes the section length that transports the sample to the instrument at the smaller flow rate to 30 cm, reducing the sampling loss rate of HOMs to less than 30 %.

As the molecules detected by the nitrate CI-APi-TOF have typically very low saturation vapor pressures, we assume that they are irreversibly lost upon contact with a surface. The diffusion coefficients D_i for each HOM_i are approximated with the expression D_i (cm^2 s^{-1}) $= 0.31 \cdot M_i^{-1/3}$, where M_i (g mol^{-1}) is the mass of the molecule. The wall loss rate inside the chamber at each temperature is determined from the following expression:

$$k_{\text{wall}}(T) = C_{\text{wall}}(T) \cdot \sqrt{D_i}, \quad (2)$$

where C_{wall} is an empirical parameter. C_{wall} is derived from dedicated sulfuric acid decay experiments at all relevant temperatures and ranges between 0.0071 and 0.0077 cm^{-1} s$^{-0.5}$ for -50 to $+25$ °C. For these experiments the measured wall loss rate and the diffusivity of sulfuric acid (0.078 cm^2 s^{-1} at

298 K and a relative humidity of 40 %) is scaled to the chamber temperature by the parameterization $(T/298\,\mathrm{K})^{1.75}$ (Hanson and Eisele, 2000). The sampling line and the sheath flow of the ion source are thermally insulated and are operated at the same temperature as the CLOUD chamber to avoid evaporation or condensation due to changes in the thermal conditions during the measurements. Note that ions formed in the CLOUD chamber, e.g., from GCRs or from the CERN pion beam, are removed by an electrostatic filter in the nitrate CI-APi-TOF inlet. Therefore, ions from the chamber do not interfere with the CI detection scheme. Finally, the sample ion signals are background corrected for a pure nitrogen sample without any VOC addition to the chamber.

2.3 PTR3-TOF

The PTR3-TOF-MS, or PTR3 for short, described in Breitenlechner et al. (2017) uses proton transfer or ligand-switching reactions from hydronium water clusters to ionize the majority of organic compounds, specifically those of which have proton affinities larger than that of the water clusters. $H_3O(H_2O)_n^+$ primary ions, produced in a corona discharge from humidified nitrogen, are transferred through a source drift region into the tripole, where the ion–molecule reactions take place. A core flow of typically 2 slm drawn from the laminar sample gas (10 slm) enters the tripole reaction region through a critical orifice. A pressure controller maintains a constant pressure of typically 70–80 hPa in the reaction region.

By applying a tunable radio frequency signal on the tripole rods, it is possible to adjust the collision energy between ions and sample gas molecules. Elevated collision energies suppress cluster ion formation of both primary and product ions but could also lead to unwanted fragmentation of certain product ions. Low collision energies on the other hand increase unwanted clustering of ions with water molecules and decrease the ionization efficiency for molecules with a proton affinity close to that of water. During CLOUD experiments we adjusted the collision energy to E/N values (E being the electric field strength and N the sample gas number density) of 62–72 Td (1 Townsend equals 10^{-17} V cm^2) by using a radio frequency (RF) of 10 MHz and an RF amplitude of 800–900 V_{pp} at a pressure of 75–77 hPa. With these settings even volatile organic compounds are detected and humidity effects are minor. Primary and product ions were analyzed with a long-TOF (LTOF, Tofwerk AG, Switzerland). All data were acquired using the TofDaq recorder by Tofwerk and analyzed with the TOF-Tracer software written by Lukas Fischer running on Julia 0.6 (https://github.com/lukasfischer83/TOF-Tracer, last access: 15 November 2019).

Precursor molecules are calibrated using a gas standard. More-oxidized molecules have typically higher proton affinities; their concentrations are estimated by using the sensitivity of 3-hexanone. Oxidized organic compounds might undergo fragmentation in reactions with $H_3O(H_2O)_n^+$ primary ions, especially when containing hydroperoxide groups (Bernhammer et al., 2017). Therefore, concentrations are lower-limit estimates.

Furthermore, data are corrected for the duty cycle transmission effects of the TOF and sampling-line losses. In Breitenlechner et al. (2017) a correction factor of 5 for the inlet line losses led to good agreement with the nitrate CI-APi-TOF for most highly oxygenated molecules containing more than five oxygen atoms in the α-pinene system (Fig. S1 in the Supplement). The compounds measured by the PTR3 span several orders of magnitude of volatility, from volatile organic compounds (VOCs) to extremely low volatility organic compounds (ELVOCs). Therefore, the correction for sampling-line losses of less oxidized molecules can only be done by changing the inlet flow rate or the fan speed inside the CLOUD chamber for each inlet temperature and testing the instrument's response for different compounds due to enhanced wall collisions. We then applied a scaled sampling-line loss correction factor ranging from 1 (no correction for VOCs, unaffected by changing the number of wall collisions) to 5 (maximum inlet correction for ELVOCs), which decreased during the tests to 20 % (or less) of their value before changed inlet flow or fan speed conditions. Molecules that contain more than five oxygen atoms are considered ELVOCs and are automatically corrected by a factor of 5 since these compounds are often too close to the detection limit of the PTR3 to get a reasonable response during the tests. Further details about the method are given in Stolzenburg et al. (2018).

2.4 Particle measurements and formation rate determination

The particle number size distributions in the size ranges between 1.2 nm and 1 µm in the chamber were measured by a series of aerosol-particle-counting instruments. The concentration of the smallest particles was measured with a particle size magnifier (PSM; Airmodus Ltd.; Vanhanen et al., 2011). The PSM was operated in scanning mode for the determination of the particle concentration at different cutoff diameters and for the particle number size distributions between 1 and 3 nm (Wimmer et al., 2013; Lehtipalo et al., 2014; Kürten et al., 2015). Additionally, a butanol condensation particle counter (CPC 3776, TSI Inc.) with a fixed cutoff diameter of 2.5 nm was used. A DMA-train (differential mobility analyzer train) measured the size distribution of particles in the 1.8 to 8 nm size range with a 10 s time resolution; it consists of six differential mobility analyzers (DMAs) with PSM or CPC detectors that are operated in parallel, each measuring a fixed size (Stolzenburg et al., 2017). A commercial nano-scanning mobility particle sizer (nSMPS 3982, TSI Inc.) resolved the particle size distribution between 8 and 63 nm. For larger particles (> 50 nm) two additional SMPS systems were used.

The ion concentration and the size distribution of charged clusters and small particles of both polarities were measured using a neutral cluster and air ion spectrometer (NAIS; Airel Ltd.; Manninen et al., 2009). This instrument determines the ion mobility distribution in the range from 0.82 to 45 nm in mobility-equivalent diameter, as well as the total particle size distribution in the size range of 2.5 to 45 nm by charging all sampled aerosols with a periodically activated corona discharge source.

The particle formation rates used in this study were determined using the full particle size distribution following the method presented in Wagner et al. (2017) and Lehtipalo et al. (2018). In practice, the particle formation rates at the cut-off diameter, 1.7 nm, were determined from the time derivatives of the total particle concentrations with diameters larger or equal to 1.7 nm. The formation rates are corrected for the particle losses in the chamber such as dilution, coagulation and wall losses.

2.5 Trace gas and water vapor measurements

Trace gas monitors were used to measure the concentration of ozone (O_3, Thermo Environmental Instruments TEI 49C), sulfur dioxide (SO_2; Thermo Fisher Scientific, Inc. 42i-TLE) and nitrogen oxides (NO, ECO PHYSICS CLD 780 TR; NO_2, CE-DOAS, University of Colorado Boulder; and CAPS NO_2, Aerodyne Research Inc.). The water vapor concentration in the chamber was monitored with a chilled dew-point mirror (Edgetech Instruments) and a direct tunable diode laser absorption spectrometer (TDL hygrometer; Werle et al., 2002).

2.6 Experimental errors

The overall scale uncertainty for the HOM and oxidation product (OVOC) measurements is +78 %/−68 %. The uncertainty in the formation rates was determined by using the error propagation method of both systematic and statistical uncertainties including those associated with the particle concentration measurement (10 %), as well as their dilution (10 %) and diffusional (20 %) losses. The statistical errors include uncertainty in $\mathrm{d}N/\mathrm{d}t$ and the coagulation sink, which varied from run to run, depending on the stability of the measurement conditions. The reproducibility (run-to-run uncertainty) under identical conditions is about 30 % as described in more detail by Kirkby et al. (2016) and Lehtipalo et al. (2018).

2.7 Volatility basis set model

The ambient temperature and the concentration of the oxidation products significantly determine their saturation vapor pressure. HOM are mainly assigned to the volatility class of LVOC and ELVOC (Bianchi et al., 2019). However, this assignment depends strongly on the temperature. Since the definition of HOM has no direct relation to the physical properties of HOMs, the volatility classification introduced by Donahue et al. (2011) is used in the present study to discuss the contribution of different HOMs and less oxidized products to NPF. In principle, the saturation vapor pressure of an organic molecule is determined by its mass and its functional groups, which affect the strength of the interaction with its neighboring molecules, and by the temperature.

The determination of the exact volatility of the oxidation products is challenging because the individual compounds cannot be isolated, as they are highly reactive and fragile species with extremely low saturation vapor pressures. However, experimentally derived volatilities from desorption thermograms measured with a FIGAERO (Filter Inlet for Gases and AEROsols) show a good agreement with the combination of semiempirical methods and theoretical model calculations (Lopez-Hilfiker et al., 2014; Schobesberger et al., 2018). This was recently verified in a complementary study of the α-pinene ozonolysis products examined here (Ye et al., 2019), in which the volatility distribution of molecules in the nucleated particles, measured with a FIGAERO inlet over a wide range of temperatures, is in good agreement with those estimated by Stolzenburg et al. (2018).

Here we follow the same approach as described in Stolzenburg et al. (2018). We combine the semiempirical group-contribution methods (SIMPOL; Pankow and Asher, 2008) with the two-dimensional volatility basis set (2D VBS) introduced by Donahue et al. (2011). It is based on the relationship between a typical molecular composition and its known volatility by parameterizing the saturation vapor pressure of an unknown molecule according to its mass and oxidation state (Donahue et al., 2012, 2013):

$$\mathrm{OS_C} = 2 \cdot \mathrm{O/C} - \mathrm{H/C}. \tag{3}$$

Therefore, the volatility can be expressed as the logarithm of the saturation mass concentration, $\log_{10} C_i^*$, from the number of carbon atoms, n_C, and oxygen atoms, n_O, within the specific molecule, i:

$$\log_{10} C_i^*\,(300\,\mathrm{K})\,[\mu\mathrm{g\,m^{-3}}] = \left(n_\mathrm{C}^0 - n_\mathrm{C}^i\right) \cdot b_\mathrm{C} - n_\mathrm{O}^i \cdot (b_\mathrm{O} - b_\mathrm{add}) - 2\frac{n_\mathrm{C}^i \cdot n_\mathrm{O}^i}{n_\mathrm{C}^i + n_\mathrm{O}^i} b_\mathrm{CO}. \tag{4}$$

Based on Donahue et al. (2011) and a revised version given in Stolzenburg et al. (2018), the parameter $n_\mathrm{C}^0 = 25$ represents the baseline carbon backbone for a volatility of $1\,\mu\mathrm{g\,m^{-3}}$ without the addition of any functional groups. The parameter $b_\mathrm{C} = 0.475$ accounts for roughly a half-order-of-magnitude decrease in saturation vapor pressure per carbon atom according to the mass of the molecule, while $b_\mathrm{O} = 2.3$ considers a more than 2-orders-of-magnitude decrease in volatility per oxygen atom assuming an equal proportion of carbonyl (=O) and hydroxyl (−OH) groups in the molecule. The carbon–oxygen nonideal interaction $b_\mathrm{CO} = -0.3$ is a nonlinearity term that adjusts the volatility estimation from

organics dominated by carbonyl (=O) and hydroxyl (−OH) groups at low O/C ratios towards HOMs, which mainly consist of hydroperoxyl (−OOH) and peroxy acid (−C(O)OH) groups at high O/C ratios. While the additional oxygen in the −OOH group ($\log C^* = -2.4$) has an almost negligible effect in reducing the saturation vapor pressure compared to the −OH group ($\log C^* = -2.2$), neither covalently bound dimers nor the ability of hydroperoxide and peroxy acid functionalities to form intramolecular hydrogen bonds are included in the nonlinear terms b_O and b_{CO} (Donahue et al., 2012; Kurtén et al., 2016). Therefore, a free parameter b_{add} is included to adjust the effect of oxygen atoms in the molecule b_O and to account for the different functionalities. To obtain this parameter, measured monomer and dimer products with known chemical composition are fitted separately with the group-contribution method SIMPOL (Stolzenburg et al., 2018). A fit to the data yields $b_{add}^{mono} = 0.904$ for HOM monomers and $b_{add}^{di} = 1.139$ for HOM dimers. Consequently, the saturation vapor pressure of any oxidation product measured in the CLOUD chamber can be estimated based on its elemental composition.

In addition, the gas-phase saturation ratio, S_i^*, for each oxidation product can be determined based on the quantitative vapor-phase measurement of the oxidized molecule concentration, $[OVOC_i]$; the molecular mass, m_i; and the associated saturation concentration, C_i^* (Donahue et al., 2013):

$$S_i^* = \frac{[\mathrm{OVOC}_i] \cdot \frac{m_i}{N_A}}{C_i^*}. \quad (5)$$

It should be noted that we can only estimate the volatility from the elemental composition, while two molecules with an identical detected mass may have different volatilities depending on their exact chemical structures and functional groups.

To account for the dependence of the volatility on temperature, T, the saturation concentration, C_i^0, can be described according to the Clausius–Clapeyron equation:

$$\log_{10} C_i^*(T) = \log_{10} C_i^0(300\,\mathrm{K}) + \frac{\Delta H_i^{vap}}{R \cdot \ln(10)} \cdot \left(\frac{1}{300\,\mathrm{K}} - \frac{1}{T}\right). \quad (6)$$

According to Donahue et al. (2011) and Epstein et al. (2009), we can approximate the evaporation enthalpy ΔH_i^{vap} as

$$\Delta H_i^{vap}[\mathrm{kJ\,mol^{-1}}] = -5.7 \cdot \log_{10} C_i^*(300\,\mathrm{K}) + 129. \quad (7)$$

Thus, a change in temperature of 15 to 20 K will result in a shift of the volatility bin by 1 order of magnitude. This study focuses mainly on the oxidation products classified as ELVOCs and ULVOCs, which will initiate cluster growth and form new particles. However, ELVOCs will condense on any particle of any size with negligible re-evaporation but may not contribute significantly to nucleation itself, while ULVOCs in contrast may efficiently nucleate. To account for our incomplete knowledge of the exact chemical structures and functional groups of the oxidation products, we assume an overall uncertainty of ±1 bin in the volatility distribution (corresponding to 1 order of magnitude in C^* at 300 K).

2.8 HOM formation and its dependence on temperature

Two parameters, AP_{oxrate}^T and γ_{HOM}^T, are used to describe and characterize the overall HOM formation. To account for the different oxidant concentration of $[O_3]$ and $[OH^\bullet]$ among the experiments and the temperature dependence of the initial reaction rate coefficient of α-pinene by these oxidants (Fig. S2a), the α-pinene oxidation rate is used as follows:

$$AP_{oxrate}^T[\mathrm{molec.\,cm^{-3}\,s^{-1}}] = k_{(AP+O_3)}^T \cdot [AP] \cdot [O_3] + k_{(AP+OH^\bullet)} \cdot [AP] \cdot [OH^\bullet]. \quad (8)$$

Here, [AP] and $[O_3]$ are the measured gas-phase concentrations of α-pinene by the PTR3 instrument and ozone by a trace gas monitor, respectively. The IUPAC-recommended rate coefficients of the α-pinene ozonolysis reaction ($k_{(AP+O_3)}^T = 8.05 \times 10^{-16} \cdot e^{-640\,\mathrm{K}/T}\,\mathrm{cm^3\,molec.^{-1}\,s^{-1}}$) and the reaction of α-pinene with $OH^\bullet$ ($k_{(AP+OH^\bullet)} = 1.2 \times 10^{-11} \cdot e^{440\,\mathrm{K}/T}\,\mathrm{cm^3\,molec.^{-1}\,s^{-1}}$) are used. The temperature dependence of these rate coefficients is shown in Fig. S2a for typical oxidant concentrations used in our experiment. The main sources of $OH^\bullet$ radicals are the ozonolysis of α-pinene and the UV photolysis of ozone. In dark conditions (UV off), the temperature-dependent ozonolysis rate is a major source of $OH^\bullet$ radicals with a yield of 80 % (Chew and Atkinson, 1996), with a resulting steady-state $OH^\bullet$ concentration of $0.5–1.6 \times 10^6\,\mathrm{molec.\,cm^{-3}}$. The formation of $OH^\bullet$ radicals depends mainly on the absolute humidity in the chamber since singlet D oxygen, which is formed during the ozone photolysis, is subsequently recombined with H_2O. The $OH^\bullet$ radical concentration by UV was estimated from dedicated actinometry experiments, forming sulfuric acid, during the same campaign. The $OH^\bullet$ production by UV yields $1–3 \times 10^6\,\mathrm{molec.\,cm^{-3}}$ at +25 °C, while at low temperatures the $OH^\bullet$ production is comparatively small ($\leq 1 \times 10^5\,\mathrm{molec.\,cm^{-3}}$ at −50 °C), due to the lower humidity in the chamber.

The total oxygenated organic fraction [OxOrg] can be estimated as follows:

$$\frac{\mathrm{d[OxOrg]}}{\mathrm{d}t} = AP_{oxrate}^T - \left(k_{dil}^T + k_{wall}^T + k_{CS}\right) \cdot [\mathrm{OxOrg}]. \quad (9)$$

The dilution loss rate k_{dil}^T is determined by dividing the total flow into the chamber by its volume ($k_{dil}^{278\,K} \sim 2 \times 10^{-4}\,\mathrm{s^{-1}}$) equaling total outflow at constant chamber pressure. Since the focus of this study is on compounds that are relevant for nucleation and early growth, we assume that oxygenated

organics are irreversibly lost due to condensation on a wall or particles. The chamber wall loss rate was determined to be $k_{\mathrm{wall}}^{278\,\mathrm{K}} = 2 \times 10^{-3}\,\mathrm{s}^{-1}$, which is the major loss. An additional loss is due to the condensation sink ($k_{\mathrm{CS}} \sim 0.001$ to $0.1 \times 10^{-3}\,\mathrm{s}^{-1}$) to particles and the dilution loss ($k_{\mathrm{dil}}^{278\,\mathrm{K}} \sim 0.2 \times 10^{-3}\,\mathrm{s}^{-1}$). The total loss rates for oxygenated organics is then $k_{\mathrm{loss}}^{278\,\mathrm{K}} \sim 2.2 \times 10^{-3}\,\mathrm{s}^{-1}$. Note that the condensation sink in the CLOUD chamber is lower than in other chamber experiments, where similar experiments have been conducted. Based on the production terms, the cumulative sinks and the total measured [HOM] by the nitrate CI-APi-TOF, the HOM yield ($\gamma_{\mathrm{HOM}}^{\mathrm{T}}$) can be expressed as

$$\gamma_{\mathrm{HOM}}^{\mathrm{T}}[\%] = \left(\frac{\frac{\mathrm{d[OxOrg]}}{\mathrm{d}t} + [\mathrm{HOM}] \cdot \left(k_{\mathrm{loss}}^{\mathrm{T}}\right)}{\mathrm{AP}_{\mathrm{oxrate}}^{\mathrm{T}}} \right) \cdot 100\,. \tag{10}$$

3 Results and discussion

3.1 Evolution of gases and particles during an experimental CLOUD run

A typical CLOUD experiment ("run") is performed after establishing a constant level of ozone. Starting from ion-free conditions, α-pinene is added to the chamber at a constant rate, as shown in Fig. 1 at 12:30 UTC, 20 October 2018. Due to chemical reactivity, the ozone concentration varied between 34 and 40 $\mathrm{ppb_v}$. As soon as α-pinene was added to the chamber, peroxy radicals ($\mathrm{RO_2^\bullet}$) and HOMs started to form. In contrast to previous CLOUD campaigns, in CLOUD12 and CLOUD13 the fan was switched to 100 % speed during the addition of α-pinene. The high fan speed increases turbulent mixing in the chamber and leads to a faster deposition of oxidation products and particles onto the wall (k_{wall}). Consequently, the steady-state concentration of condensable material (ELVOCs and ULVOCs) was shifted well below the nucleation threshold by increasing the fan speed from its standard value (12 %) to 100 %. The concentration of the peroxy radicals measured by the CI-APi-TOF, however, is not much affected by the strong fan mixing. Reaction rate constants for highly functionalized $\mathrm{RO_2^\bullet}$ from α-pinene self- and cross-reactions are in a range of 1 to $10 \times 10^{-11}\,\mathrm{cm^3\,molec.^{-1}\,s^{-1}}$ at 300 K (Berndt et al., 2018a). Due to their high reactivity, the lifetime of the $\mathrm{RO_2^\bullet}$ radicals is mainly determined by chemical loss rates and relative weakly by the wall loss rate.

After the precursors reached a steady-state concentration (13:23 UTC in Fig. 1), the mixing fans were switched from 100 % to 12 % speed, reducing HOM and cluster wall loss rates by a factor of 2 to 3. Consequently, a new steady-state concentration of α-pinene oxidation product monomers (C_{10}) and dimers (C_{20}) was established on the wall loss timescale. Due to the increased gas-phase concentration of condensable material, a NPF event was initiated. Molecular clusters started to form and grew into aerosol particles. After the particle formation rate had reached a steady state under neutral conditions (J_{n}), the HVCF inside the chamber was turned off (15:38–17:40 UTC in Fig. 1). Due to natural ionization at intensities of ground-level GCRs, the ion concentration increased to $> 1000\,\mathrm{cm^{-3}}$. Maintaining all other chamber parameters as constant, we observed an enhancement of up to 2 orders of magnitude or more in the nucleation rate of new particles due to ion-induced cluster stabilization (J_{gcr}; Kirkby et al., 2016).

During some stages, the UV light was also turned on to study its effect on the oxidation chemistry by comparing the results with (06:00–08:20 UTC in Fig. 1) and without (03:09–05:41 UTC in Fig. 1) photochemical reactions under otherwise identical conditions. The particle formation sequence was then repeated at various concentrations of α-pinene and different temperatures over the range of atmospheric interest. In the data analysis, we assume that the particles observed at a 1.7 nm mobility diameter are stable against evaporation and serve as a valid proxy for NPF in the chamber.

3.2 Effect of temperature on α-pinene oxidation and HOM formation

Temperature has a strong effect on peroxy radical isomerization and, consequently, on the production rate of closed-shell oxygenated products. HOM formation is, in principle, controlled by the production rate and lifetime of the precursor peroxy radicals, while the lifetime of the radicals is determined by the competing reaction of the unimolecular autoxidation and the bimolecular terminations. The unimolecular H-shift reaction has a much higher pre-exponential term for the rate constant given by the molecular vibration frequencies compared with that for the bimolecular process, which mainly depends on the bimolecular collision frequency (Praske et al., 2018). However, the higher activation energy barrier of the H-shift reaction partly or fully compensated this. Quantum chemical calculations for different $\mathrm{RO_2^\bullet}$ radicals from α-pinene oxidation suggest activation energies between 92 and 121 $\mathrm{kJ\,mol^{-1}}$ for the autoxidation process (Rissanen et al., 2015). Because of this high activation energy barrier, temperature has a substantial effect on the intramolecular H shift and will strongly reduce the autoxidation at lower temperature. In contrast, the temperature dependence of the bimolecular reaction (like molecular dimer formation) is much weaker or, in some cases, even exhibits a slightly negative dependence. Consequently, the competition at lower temperatures between the termination reaction and the slower unimolecular autoxidation rate influences the oxidation state of the products and their distribution. This temperature dependence of the α-pinene oxidation was previously observed in the composition of naturally HOM ions, charged by cosmic rays in the CLOUD chamber (Frege et al., 2018), and is confirmed here for neutral HOMs and their gas-phase clusters, as shown in Fig. 2. A strong decrease in the mean O/C ratio of the detected oxidation products can

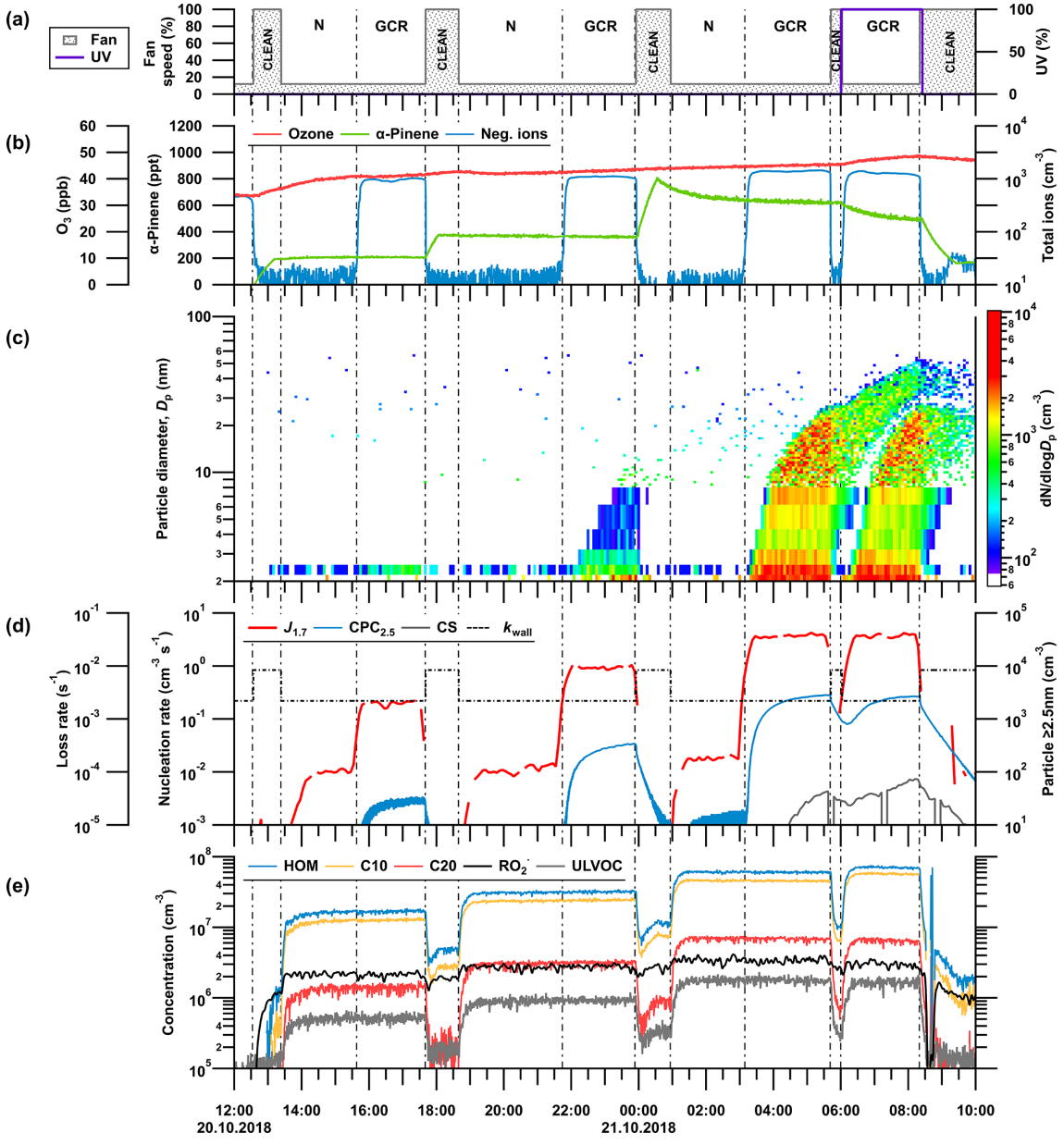

Figure 1. Typical CLOUD experiment sequence of a NPF experiment by α-pinene oxidation for three different precursor concentrations. The figure shows an example α-pinene NPF run during the CLOUD13 campaign. The experiment is conducted at a temperature of +5 °C and at a relative humidity of 80 %. The vertical lines indicate a change in the experimental conditions in the chamber (e.g. change in settings for fan speed, UV illumination, clearing field) marking a new stage within the run. **(a)** Change in fan speed and UV light intensity during the run. N, GCR and CLEAN indicate neutral (high-voltage clearing field on), galactic cosmic ray (high-voltage clearing field off) and cleaning (neutral periods including high fan speed to clean the chamber of particles) conditions, respectively. **(b)** Time series of ozone, α-pinene and negative ions. **(c)** Combined size distribution of aerosol particles measured by the DMA-train (1.8–8 nm) and nanoSMPS (8–63 nm). **(d)** Evolution of the nucleation rate at 1.7 nm ($J_{1.7}$) and the total particle concentration above 2.5 nm, measured with a scanning PSM (1.7 nm) and a butanol-based CPC (2.5 nm). Furthermore, the loss rates to the chamber walls (k_{wall}, dashed black line) and the determined particle condensation sink (CS, gray line) are shown. **(e)** Evolution of total HOM concentration and partitioning into HOM monomers (C_{10}), HOM dimers (C_{20}) and peroxy radicals ($RO_2^{\bullet}$) as well the fraction of ultralow-volatility organic compounds (ULVOCs) measured by the nitrate CI-APi-TOF.

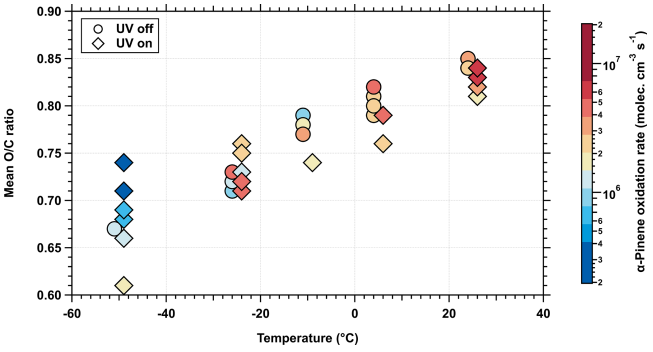

Figure 2. Mean oxygen-to-carbon (O/C) elemental ratio of HOMs at different temperatures and various α-pinene oxidation rates. Mean O/C ratio of HOMs detected by the nitrate CI-APi-TOF. HOMs are produced from a mixture of α-pinene (200–2000 ppt_v) and ozone (37–48 ppb_v) under dark (circles) and UV-illuminated (diamonds) conditions at five different temperatures ranging from -50 to $+25\,^{\circ}C$. The marker symbols are slightly horizontally shifted on the x axis to ensure a better visibility. The higher $OH^{\bullet}$ radical concentration due to the UV light influences the oxidation state of the HOM. The different initial precursor concentrations lead to only a minor effect on the oxidation ratio. Temperature has an impact on the formation of HOM closed-shell products as the autoxidation proceeds more slowly at lower temperatures.

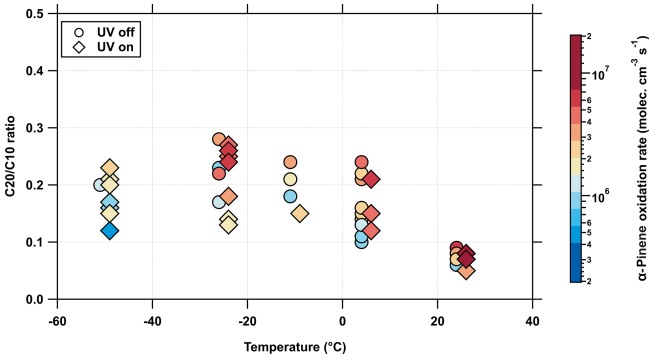

Figure 3. Mean C_{20}-dimer-to-C_{10}-monomer ratio of α-pinene oxidation at different temperatures. The ratio of the detected sum of dimer products (C_{20}) versus the sum of monomer products of the α-pinene oxidation experiment measured by the nitrate CI-APi-TOF. The color bar indicates the α-pinene oxidation rate. Elevated oxidation rates result in a stronger increase in dimer products than monomer products due to more $RO_2^{\bullet}$–$RO_2^{\bullet}$ reactions. While the ratio between monomers and dimers is stable for low temperatures ($< 0\,^{\circ}C$), it decreases with higher temperatures. This is an indication that some of the monomers are semivolatile at higher temperatures and do not irreversibly condense on a cluster or particle. Also, the bimolecular termination of the autoxidation, due to an elevated concentration of $OH^{\bullet}$ radicals, can cause this effect. No pronounced effect due to the different ion concentration in the chamber experiments can be recognized.

be observed as temperature decreases. This decrease in O/C ratio with decreasing temperature was also observed in the particle phase by Kristensen et al. (2017) and Ye et al. (2019) and raises the question of the extent to which the reduction in oxidation also affects NPF.

In general, the HOM production rate is approximately linearly dependent on its initial precursor concentration, while the bimolecular termination of the $RO_2^{\bullet}$ radicals increases with a squared dependency. Molteni et al. (2019) showed that an increase in the α-pinene oxidation rate, and thus an increase in the $RO_2^{\bullet}$ radical concentration, leads to a slightly lower mean O/C ratio of the detected products. However, this effect is rather small at low α-pinene oxidation rates ($< 1 \times 10^7$ molec. $cm^{-3}\,s^{-1}$) and could not be clearly recognized in our data.

However, a similar effect of $RO_2^{\bullet}$ radical concentration on the bimolecular terminations can be seen in the mean HOM dimer-to-monomer (C_{20}-to-C_{10}) ratio in Fig. 3. An elevated oxidation rate (AP^{T}_{oxrate}, color scale) leads to a slightly increased HOM dimer formation. In addition, Fig. 3 shows that the ratio of HOM dimers to monomers is almost unaffected at lower temperatures and depends mostly on the formation of $RO_2^{\bullet}$ radicals. This result also indicates that the bimolecular termination has only a minor temperature dependence.

At temperatures below $0\,^{\circ}C$, the ratio of dimers to monomers is about 20 %. It should be noted that, especially at the lowest temperatures ($-50\,^{\circ}C$), dimer clusters from traditional oxidation products are formed, e.g., pinonic acid dimers, which do not result from the autoxidation reaction (non-HOM dimer clusters). Due to lower fragmentation in the instrument, these dimers can also be detected by the mass spectrometer. Since we cannot differentiate between them, these dimer clusters are included in the overall gas-phase HOM dimer concentration. However, due to their greatly reduced saturation vapor pressure, these dimers also participate in NPF.

At temperatures above $0\,^{\circ}C$, the gas-phase HOM monomer concentrations increase more than the HOM dimer concentration, as seen from the decreasing dimer ratio of 20 % to less than 10 % (Fig. 3). This shift can be explained by two factors: volatility and formation rate. At higher temperatures, the saturation vapor pressures of the HOM monomers are sufficient for them to re-evaporate from surfaces (or particles), while the dimers remain, essentially irreversibly. This shift in saturation vapor pressure is also consistent with volatility predictions by the VBS model, as shown by the color code in Fig. 5. This supports our conclusion that the HOM dimers of accretion reactions play a decisive role in NPF, especially at higher temperatures (Mohr et al., 2017; Lehtipalo et al., 2018).

At higher temperatures, the concentration of $HO_2^{\bullet}$ radicals can also strongly increase, as shown by the $HO_2^{\bullet}$ reaction rate coefficients in Fig. S2b. In addition to their formation by alkoxy radicals ($RO^{\bullet}$), the $HO_2^{\bullet}$ radicals are mainly formed by the reaction of $OH^{\bullet}$ radicals with ozone, while the $OH^{\bullet}$ radical concentration depends mainly on the ozonolysis re-

action rate of α-pinene. Both reactions have a positive temperature dependence. The higher concentration of $HO_2^\bullet$ leads to an increased competition with the $RO_2^\bullet$–$RO_2^\bullet$ self-reaction, which reduces the formation of HOM dimers and increases HOM monomers.

To summarize, the reduced α-pinene ozonolysis rate at lower temperatures leads to lower concentrations of HOMs. Furthermore, due to the strong temperature dependence of the initial H shift in peroxy radical isomerization, the HOM yield per ozonolysis reaction will also be reduced. As shown in Fig. 4a, the overall HOM yield drops dramatically as the temperature decreases. From the slopes of the linear fits of HOM measurement by the nitrate CI-APi-TOF (Fig. 4b), the total HOM formation of the α-pinene oxidation reactions (O_3 and $OH^\bullet$) provides the following HOM yields: $\gamma_{HOM}^{298\,K} = 6.2\,\%$ at 25 °C, $\gamma_{HOM}^{278\,K} = 4.7\,\%$ at 5 °C, $\gamma_{HOM}^{263\,K} = 2.9\,\%$ at −10 °C, $\gamma_{HOM}^{248\,K} = 1.3\,\%$ at −25 °C and $\gamma_{HOM}^{223K} = 0.7\,\%$ at −50 °C. Whereas these yields at 25 and 5 °C are consistent with earlier publications (Ehn et al., 2014; Jokinen et al., 2015; Kirkby et al., 2016), here we extend the HOM yields to much colder temperatures. However, Quéléver et al. (2019) report a much stronger temperature dependence of the HOM yields with decreasing temperature, which may result from a combination of differences in the experimental and instrumental conditions between the two studies. It is important to note that the HOMs require at least six oxygen atoms (Fig. S1); otherwise, the nitrate ionization scheme cannot fully detect them. The unimolecular reaction of the $RO_2^\bullet$ radicals proceeds at much slower rates at low temperatures, due to the height of the reaction barrier, while the bimolecular termination of the radicals is much less affected by the temperature (Ziemann and Atkinson, 2012; Frege et al., 2018). Therefore, at low temperatures, there is a higher chance that an $RO_2^\bullet$ radical will be lost before it reaches a high oxygenation level and forms a HOM that can be detected by the nitrate CI-APi-TOF. Besides the termination reactions, relevant loss mechanisms of $RO_2^\bullet$ radicals are wall loss and uptake on particles. Especially under cold conditions, it becomes more likely that organic molecules with fewer than six oxygen atoms can condense on preexisting or newly formed particles due to their reduced volatility and can thereby increase the condensation sink compared to at high temperatures. As a result, the HOM yield drops significantly depending on the condensation sink, which tends to result in lower determined yields, especially at low temperatures.

3.3 Change in the volatility distribution of α-pinene oxidation products as a function of temperature

Despite the decrease in the total HOM yield, Fig. 4c shows an increase in ultralow-volatility products, indicating a more important reduction in the saturation vapor pressure of all oxidation products compared with the reduction in their oxidation states. The definition of HOM is based on the chemical composition and is temperature independent, whereas the

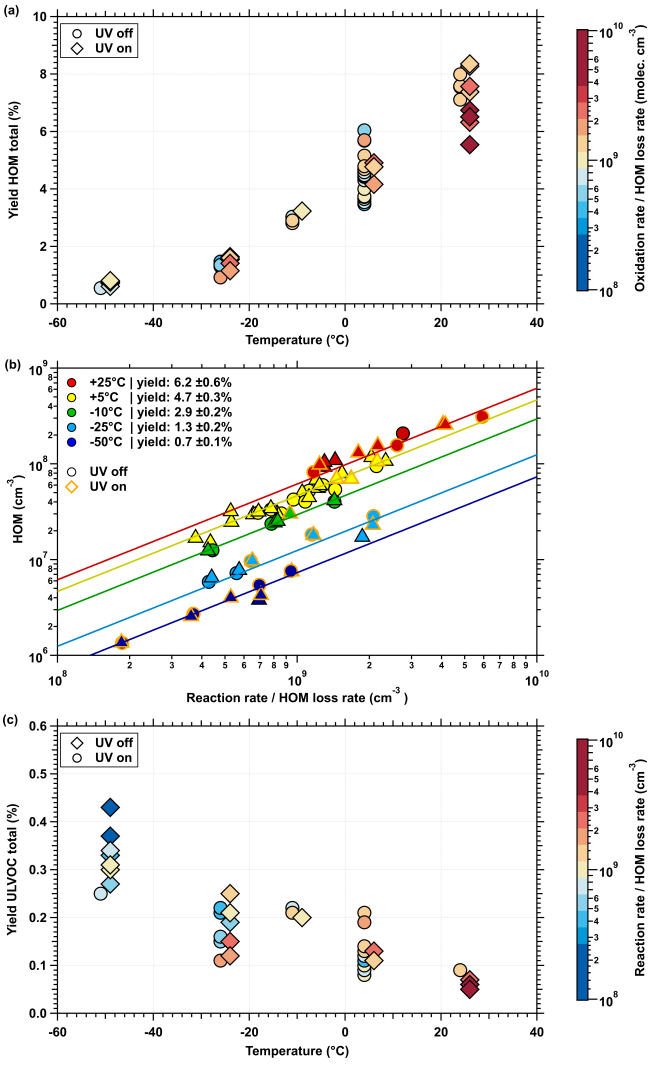

Figure 4. Total HOM and ULVOC yields as a function of α-pinene oxidation rates at five different temperatures. The total gas-phase **(a)** HOM and **(c)** ULVOC yields measured by the nitrate CI-APi-TOF according to Eq. (10). The color code in panels **(a)** and **(c)** as well as the x axis in panel **(b)** shows the oxidation rate corrected for all losses and condensation sinks inside the chamber. **(a)** The total HOM yield decreases with decreasing temperature, while the ULVOC yield **(c)** increases. The marker symbols for dark (circles) and UV-illuminated (diamonds) conditions are slightly horizontally shifted on the x axis to ensure a better visibility. **(b)** The mean yields are derived from the slope of the linear fits of the HOM concentrations at the different temperatures. The measured HOM concentration is linearly dependent on its precursor concentration (oxidation rate) as indicated by the double-logarithmic fits with the slope of 1. Thus, there is neither a saturation effect in the chemical production rate nor an instrumental effect at all temperatures. Overall systematic scale uncertainties of ±40 % for the α-pinene reaction rates and +78 %/−68 % for the HOM mixing ratios are not shown.

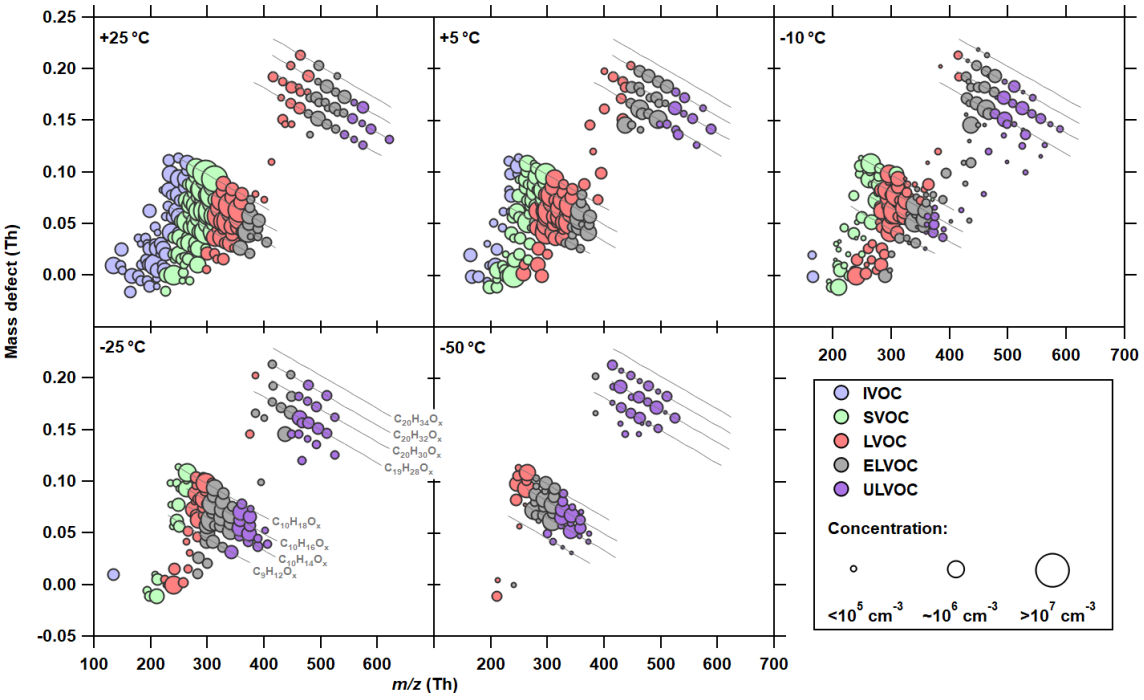

Figure 5. Molecular composition of neutral HOMs at the five temperatures studied and their corresponding volatility. Mass defect (difference of exact mass to integer mass) versus m/z of gas-phase HOMs measured with the nitrate anion CI-APi-TOF. Data shown represent steady-state run conditions (production term balanced with all loss rate). For clarity, signals other than organics, such as the reagent ions, are not shown in the plot. Each circle represents a particular molecular composition. All molecules shown here are clustered to a nitrate ion monomer from the reagent ion chemical ionization. Same oxidation products clustered to different reagent ions (e.g., $(HNO_3)NO_3^- \cdot C_{10}H_{14}O_7$) are summed to the reagent monomer cluster ion ($NO_3^- \cdot C_{10}H_{14}O_7$). Similar α-pinene oxidation rates (2–3 $\times$ 10^6 molec. cm^{-3} s^{-1}) are used for each temperature to ensure better comparability. The area of the markers is proportional to the logarithm of the concentration measured by the nitrate CI-APi-TOF. The systematic scale uncertainty on the HOM concentrations is +78 %/−68 %. The lines represent a homologous group of oxidation products with the same hydrogen-to-carbon (H/C) elemental ratio but with an increasing oxygen level (e.g., $C_{10}H_{14}O_{3-12}$). The group between 240 and 420 Th is referred to as HOM monomers (mainly C_8–C_{10}), while the band between 400 and 620 Th marks HOM dimers (mainly C_{18}–C_{20}). The color indicates the corresponding volatility range based on the volatility basis set (VBS) model. ULVOC, ultralow-volatility organic compound (purple; $C^*(300\,K) < 3\times10^{-9}$ µg m^{-3}); ELVOC, extremely low volatility organic compound (gray; $3\times10^{-9} < C^*(300\,K) < 3\times10^{-5}$ µg m^{-3}); LVOC, low-volatility organic compound (orange; $3\times10^{-5} < C^*(300\,K) < 0.3$ µg m^{-3}); SVOC, semivolatile organic compound (green; $0.3 < C^*(300\,K) < 300$ µg m^{-3}); IVOC, intermediate-volatility organic compound (blue; $300 < C^*(300\,K) < 3\times10^6$ µg m^{-3}).

physical properties, in particular the volatility, do depend on temperature. Therefore, the classification of a molecule as HOM is inadequate for describing its nucleation properties over a wide temperature range. Figure 5 shows a mass defect plot of the oxidation products measured with the nitrate CI-APi-TOF, where the color code classifies them into the different volatility bands according to the calculated saturation vapor pressures at each temperature. According to Sect. 2.7, the volatility classes are based on a semiempirical approach of the two-dimensional volatility basis set (2D VBS) model (Donahue et al., 2011). The area of the markers reflects the measured concentrations. Only experiments with a similar AP^T_{oxrate} (2–3 $\times$ 10^6 cm^{-3}) are included, to ensure comparability in terms of α-pinene oxidation rates and their temperature dependence. The reduction in the mean oxidation state (OS_C) with decreasing temperature is indicated by the shift of the detected products to the left-hand edge (lower masses) of the different homologous sequences of oxidation products, shown by the lines in Fig. 5 and the coloring in Fig. S3.

As seen in the 25 °C data in Fig. 5, most HOM monomers belong to the low-volatility (LVOC) or even semivolatile (SVOC) class, which corresponds to the model results of Schervish and Donahue (2020). Therefore, the loss rate of these oxidation products from the gas phase is low compared to the extremely low volatility products (ELVOCs), which has already been discussed based on the HOM dimer-to-monomer ratio in Fig. 3. At 25 °C, only the most oxygenated monomers have an extremely low saturation vapor pressure, while none of them fits the ULVOC class. However, the majority of ELVOCs and ULVOCs at 25 °C are HOM dimers. As temperature decreases, the saturation vapor pressures of the HOM monomers shift towards the ELVOC class, despite

the decrease in their O/C ratios. Consequently, at −50 °C, almost all the α-pinene oxidation products detected by the nitrate CI-APi-TOF are ELVOCs or ULVOCs.

When the concentration of an oxidation product exceeds its saturated vapor concentration, it becomes supersaturated (saturation ratio, $S_i > 1$). The saturation ratio of an oxidation product, therefore, indicates to what extent this individual product can condense from the gas phase and contribute to NPF and growth. Based on the measured concentrations and the volatilities derived from the VBS model, the steady-state saturation ratios for each individual compound (a mixture of isomers) can be determined according to Eq. (5). Accordingly, the saturation ratio, S_i, for each identified oxygenated molecule (HOM_i) is given by the area of the marker in Fig. 6. This presentation gives an indication of the ability to form embryonic molecular clusters by the different HOM_i's as a function of temperature. Nucleation requires vapors with $S_i \gg 1$, since they must overcome the Kelvin (curvature) barrier. The color code in Fig. 6 indicates the concentration determined by the nitrate CI-APi-TOF.

Due to their low volatility, the highest oxidation states of the reaction reach high levels of supersaturation. However, their total concentrations are low, so their abundance is likely to be insignificant for the formation of clusters and subsequent growth. Consequently, the nucleation and initial growth rate may be limited for each individual HOM. Therefore, further support from other condensable gases, such as sulfuric acid and ammonia, may be required to grow these clusters to larger sizes before they are lost to walls or preexisting particles. However, by summing up the saturation ratios, S_i, of all oxidation products, the nucleation ability can be estimated. Based on the −25 °C data in Fig. 6, the proportion of the supersaturated monomers is significantly higher than that of the supersaturated monomers at higher temperatures. Thus, despite the decrease in oxidation rate, it is expected that the decrease in volatility with decreasing temperature will increase nucleation and initial growth rates at given precursors (see Sect. 3.5).

3.4 CI-APi-TOF HOM detection and the combination of the PTR3 data set

Nitrate chemical ionization mass spectrometry quantitatively measures highly oxygenated organic molecules with a high O/C ratio (Hyttinen et al., 2017; Ehn et al., 2017). We generally assume that the charging efficiency in the instrument for HOMs is equal to that of sulfuric acid. We also assume that the charging efficiency does not change significantly at different temperatures and humidity (Viggiano et al., 1997) but is mainly influenced by the oxidation state of the oxidized volatile organic compounds (OVOCs).

Kinetic simulations by Hyttinen et al. (2017) show that, for nitrate chemical ionization, HOMs are typically charged with the monomer of the reagent ions $HOM_i \cdot NO_3^-$, since this cluster has a stronger binding energy than the dimer or trimer of the reagent ions, $(HNO_3)_{1-2}NO_3^-$. However, we find that a small fraction (∼ 10 %) of the HOMs do cluster with the dimer of the reagent ions. At low temperatures, this fraction increases due to the increased stability of the charged clusters, resulting in an enhanced survival probability of the charged nitrate dimer in the CI-APi-TOF. At −50 °C, some of the detected HOMs even form clusters with the trimer of the reagent ions. The low oxidation states of the α-pinene oxidation products were most efficiently detected with a nitrate dimer ion. Hyttinen et al. (2015) showed that the HOMs formed from cyclohexene oxidation require at least two hydroperoxy groups, or other H-bond-donating groups, in order to form an energetically more favorable cluster than the nitrate dimer or trimer ion cluster. The reason why bonding of low-oxidation products to the reagent dimer or trimer ion cluster is preferred is probably the distance between the interacting functional groups of the oxidation product and the size of the reagent ion itself. As shown by Rissanen et al. (2015), the primary ozone attack in α-pinene oxidation results in a ring-opening reaction, leading to a subsequent carbon-centered alkyl-type radical bearing functional groups at both ends of the molecule. Due to the distance between these functional groups, a single nitrate anion can only interact with one of the hydroperoxy groups, while the dimer or trimer reagent ion can bridge this distance and form an energetically more stable ion cluster.

Since both the oxidation state and the saturation ratio of the oxidation products depend on temperature, some of the less oxygenated but nevertheless highly supersaturated OVOCs may be underestimated or even undetected by a nitrate CI-APi-TOF. Figure 6 should therefore be considered to show a lower limit at low temperatures (−25 and −50 °C), where most oxidation products have a low O/C ratio. Furthermore, the saturation ratio of the oxygenated dimer products (C_{20}) may be underestimated, even at relatively high temperatures, due to their generally lower O/C ratio.

The PTR3 instrument, which uses H_3O^+ reagent ions, is well suited to measure the less highly oxygenated products. Figure S1 shows a comparison of the homologous groups of $C_{10}H_{14,16}O_x$ measured with both instruments. The concentration of HOM dimers did not exceed the limit of detection (LOD, 8×10^5 cm^{-3}) of the PTR3 instrument. Therefore, no direct statement can be made here about the concentration and saturation ratio of the less oxygenated dimer products. However, as the concentrations are below the LOD, even though they can initiate NPF, they may provide only a small amount of condensable mass to promote early growth. As pointed out in Stolzenburg et al. (2018), the concentration of products with an O/C ratio of 0.6 to 0.7 is in good agreement between the two instruments, as shown in Fig. S1, while the nitrate CI-APi-TOF lacks the less oxygenated products. The different color segments on the lower axes, however, show that the nitrate CI-APi-TOF can quantitatively measure the products, especially the ELVOC and ULVOC products at mixing ratios in the parts-per-quadrillion-by-volume range.

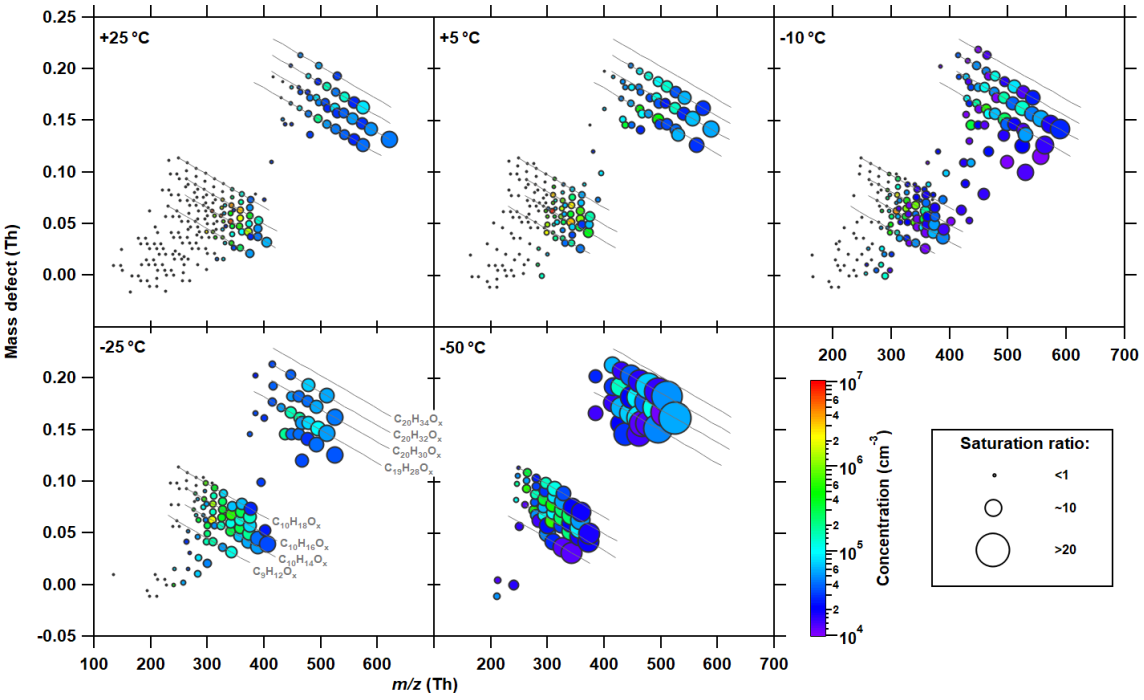

Figure 6. Composition of the measured gas-phase HOMs at different temperatures and their saturation ratio distribution. Same α-pinene oxidation rates (2–3 $\times$ 10^6 molec. cm^{-3} s^{-1}) and run conditions as shown in Fig. 5. The area of the markers is proportional to the saturation ratio of each detected HOM in the gas phase as measured by the nitrate CI-APi-TOF, while the color reflects the measured concentration. The figure directly shows the molecules that drive the nucleation and early growth of embryonic clusters. Note that the concentrations of less oxidized products are likely underestimated by the nitrate CI-APi-TOF and should therefore be interpreted as a lower limit. The lines represent a homologous group of oxidation products with the same H/C ratio but a different number of oxygen atoms.

Since the ULVOCs are the most effective molecules for nucleation (Schervish and Donahue, 2020), the nitrate ionization instrument provides a comprehensive molecular understanding of NPF over a wide range of tropospheric temperatures.

Figure 7 shows all oxidation products distributed according to their volatility (in bins of factors of 10) measured by the nitrate CI-APi-TOF and PTR3 instruments at each temperature. While these data are consistent with the results of Stolzenburg et al. (2018), the present study covers a wider temperature range from -50 to 25 °C. The dashed lines in Fig. 7 represent the cumulative concentrations, starting with the lowest-volatility products measured by the nitrate CI-APi-TOF. The solid lines include the less highly oxygenated products measured by the PTR3 instrument, assuming the same volatility products for each bin. While the nitrate CI-APi-TOF can completely quantify the ULVOC and ELVOC class at temperatures ≥ -25 °C, the molecules measured by the PTR3 contribute to the total ELVOC class at the lowest temperature (-50 °C). The ULVOC class is fully represented by the nitrate CI-APi-TOF and is anticorrelated with temperature, as already shown in Fig. 4c. Furthermore, Fig. 6 shows that, at low temperatures (-50 and -25 °C), almost all oxidation products detected by the nitrate CI-APi-TOF are supersaturated at the indicated precursor concentration and can form stable embryonic clusters and small particles. Due to the intense decrease in volatility at these low temperatures, a large fraction of the less oxygenated molecules also falls in the ELVOC class. While the ULVOC and ELVOC molecules are evenly distributed over a wide range of volatility bins, an uncertainty in the saturation concentration of 1 order of magnitude would not alter this conclusion.

3.5 Effect of temperature on pure biogenic nucleation

The decrease in HOM volatility at reduced temperatures has a strong effect on the particle formation rates at 1.7 nm ($J_{1.7}$), as shown in Fig. 8. Despite the decrease in autoxidation rate of the peroxy radicals and the associated reduction in HOM yields at lower temperatures, the reduced volatility counteracts this effect and leads to an overall increase in particle formation rate.

Figure 8a presents the particle formation rate as a function of the total HOM concentration measured by the nitrate CI-APi-TOF. This figure shows that the same or higher nucleation rates are reached for HOM concentrations a factor of 100 lower at -50 °C compared to 25 °C. At low temperatures, molecules with less oxygenation can achieve the same formation rate as more highly oxygenated molecules at higher temperatures. However, the chemical definition of

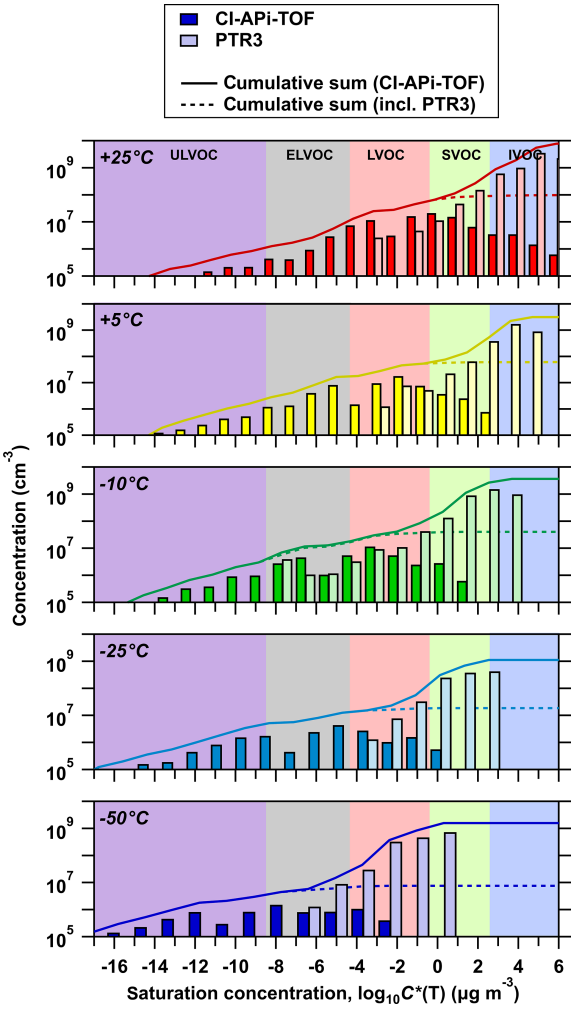

Figure 7. Volatility distribution of the measured oxidation products for five representative temperatures. The mass concentration and volatility distributions of oxidation products shown here are at the same α-pinene oxidation rates (2–3 $\times$ 10^6 molec. cm^{-3} s^{-1}) and run conditions as data shown in Fig. 5. The summed oxidation product concentration of each volatility bin is divided into the nitrate CI-APi-TOF (dark color) and the PTR3 instrument (light color). Each volatility bin is defined at 300 K, shifted and widened according to its corresponding temperature. The highest and lowest bin are overflow bins. The solid lines for each temperature represent the cumulative sum of the volatility bins of both instruments towards higher volatility, while the dashed line represents the nitrate CI-APi-TOF only. Oxidation products detected by the nitrate CI-APi-TOF (LOD $\leq 5\times10^4$ molec. cm^{-3}) below 1×10^5 molec. cm^{-3} are added to the cumulative sum. This results in slightly higher concentrations of the cumulative sums when compared with the first visible bin. The color bands in the background indicate the volatility regimes as in Donahue et al. (2012) and Schervish and Donahue (2020).

HOM does not reflect the saturation vapor pressure of the oxidation products. This representation therefore underestimates the condensable mass at low temperatures where the high gas-phase concentration of the less oxygenated products can contribute to sufficient supersaturation and NPF (see Sect. 3.4).

The total HOM concentration depends mainly on the C_{10} monomer concentration, while the C_{20} dimers only account for 10 % to 20 % of that total, depending on the experimental conditions (e.g., $HO_2^{\bullet}/RO_2^{\bullet}$, temperature, precursor concentration). Whereas most of the C_{10} monomers have a saturation vapor pressure in the range of SVOC to LVOC at high temperatures ($> 5\,^{\circ}$C), at a low temperature ($-50\,^{\circ}$C) almost all of them belong to the ELVOC and even the ULVOC class. At higher temperatures, dimerization (C_{20} formation) can be the rate-limiting step for NPF since the volatility depends not only on the polarity of the molecule (functional groups) but also on its size (m/z). Thus, a major fraction of the HOM dimers belongs in the ELVOC to ULVOC range, even at 25 °C (see also Fig. 5). Therefore, the ULVOC class may provide a more appropriate proxy to parameterize nucleation rates from monoterpene oxidation. Note that dimer clusters (noncovalently bonded clusters) may form at lower temperatures ($< -25\,^{\circ}$C), which, despite their low degree of oxidation, also have a low saturation vapor pressure, and so may contribute both to NPF and to the total dimer concentration.

The continuous decrease in the autoxidation rate coefficient with decreasing temperatures reduces the HOM concentrations in Fig. 8a, for the same precursor concentrations used at higher temperatures. Therefore, Fig. 8b shows the NPF rate as a function of the sum of all molecules in the ULVOC range. The evaporation rate of a cluster containing two ULVOCs will conceptually be related to the average volatility of those two molecules. Due to the sufficiently low saturation vapor pressure, we consider the ULVOC range to be the volatility range where it is increasingly likely that a cluster will grow, not evaporate, and thus nucleate. This is consistent with the result shown in Fig. 8b as it unifies the NPF rates at all temperatures and shows that ULVOC concentration provides a better proxy compared to the total HOM concentration. Ideally, all lines of the nucleation rates for the different temperatures would coincide into a single line in Fig. 8b. However, the nucleation rate will still likely be a function of volatility within the ULVOC (and partially the ELVOC) range. Based on the previous discussion, however, we can infer that both mass spectrometers underestimate some low-volatility products, especially at the two lowest temperatures. Fragmentation and/or clustering of the oxygenated molecules inside the mass spectrometers could also lead to misinterpretation of their volatility (Passananti et al., 2019). In addition, the temperature dependence of the volatility classification is subject to larger uncertainty as the temperature decreases. Thus, we estimate that the bin assignment is uncertain by about one bin (a factor of 10 in volatil-

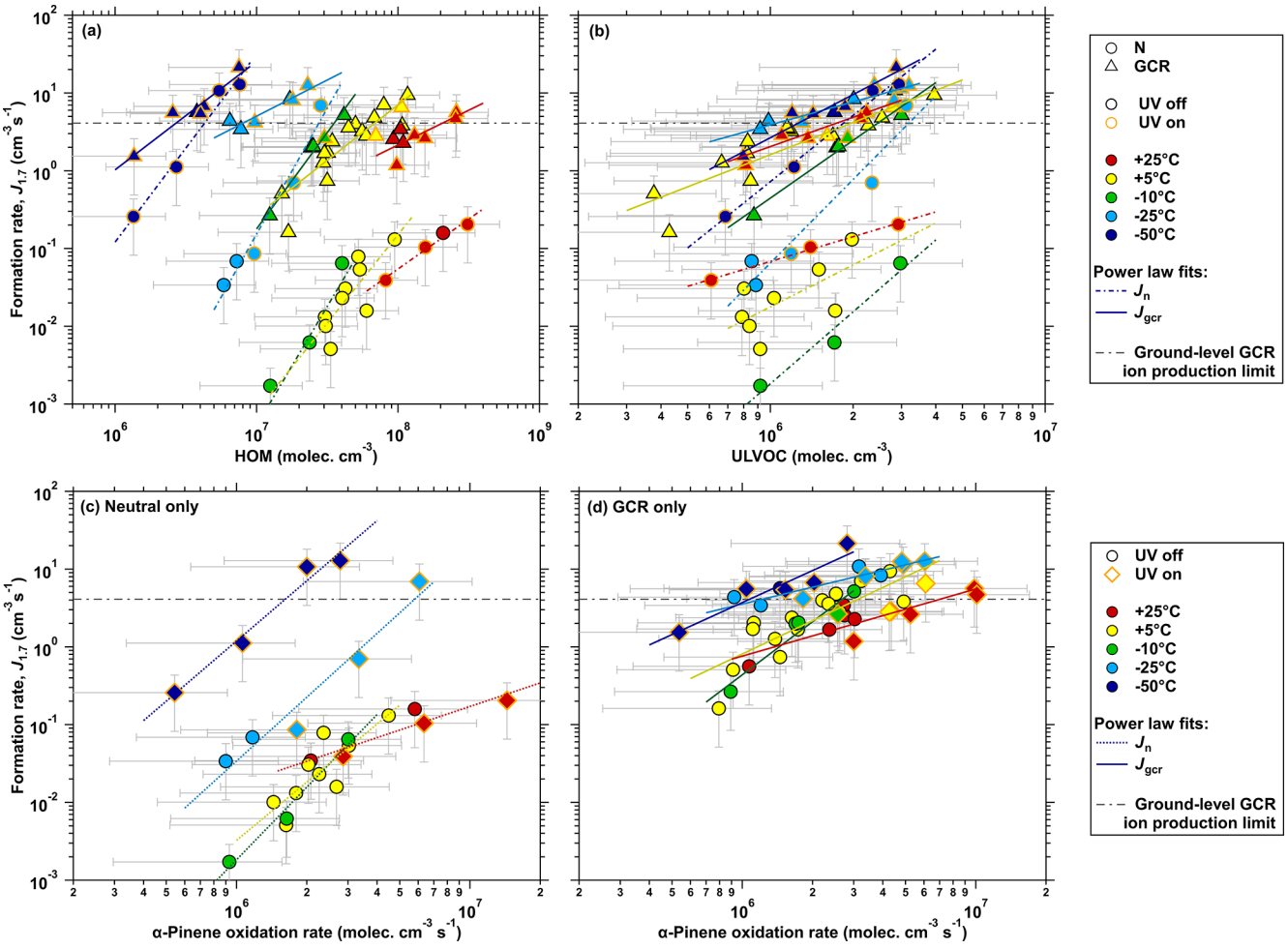

Figure 8. NPF rate as function of HOM, ULVOC and α-pinene oxidation rates for temperatures from -50 to $+25\,^{\circ}$C. Biogenic NPF rates at 1.7 nm ($J_{1.7}$) of α-pinene oxidation versus **(a)** total measured gas-phase HOMs and **(b)** ULVOC concentration under ion-free (J_n, circles) and charged (J_{gcr}, triangle) conditions. The color of the marker points specifies the investigated temperatures. The experimental conditions are 200–2000 ppt$_v$ of α-pinene, 37–48 ppb$_v$ of O_3, relative humidity 40 %–90 % and $< 1 \times 10^5$ cm^{-3} H_2SO_4. Black marker outlines indicate dark conditions, while orange marker outlines represent UV-illuminated conditions. Dash-dotted lines (J_n) and solid lines (J_{gcr}) are power law fits of the distinct ion condition for each of the individual temperatures. The dark gray dash-dotted line indicates the upper limit of ion-induced nucleation (J_{iin}) from the GCR ion-pair production rate at ground level. **(c)** Neutral (J_n) and **(d)** charged (J_{gcr}) NPF rate as a function of α-pinene oxidation rates under dark conditions (circles) and UV-illuminated conditions (diamonds). The bars indicate 1σ total errors, although the overall systematic scale uncertainty of $+78\,\%/-68\,\%$ in the HOM mixing ratios is not shown.

ity). Further, the stabilizing effect of ions is not considered in the VBS model. Under ion-free conditions, the pure biogenic nucleating clusters are generally less stable against evaporation. It is possible that the stabilizing effect of an ion essentially shifts the relevant volatility range by some number of bins and results in a larger uncertainty at warm temperatures, while this effect is less apparent at colder temperatures in absence of any ions for the same ULVOC concentration. The probability that a cluster grows under ion-free conditions, due to an arriving molecule, is strongly dependent on its volatility compared to GCR conditions. Therefore, the exact volatility distribution can also be important within the ULVOC class, especially for the neutral conditions.

Figure 8c shows the neutral particle formation rates at 1.7 nm (J_n) and Fig. 8d the ion-induced particle formation rates by galactic cosmic rays ($J_{gcr} = J_n + J_{iin}$) as a function of the α-pinene oxidation rate (AP^T_{oxrate}). This representation accounts for the change in the oxidation rate coefficient of α-pinene with respect to temperature and is independent of the concentration of the oxidation products and their uncertainties in detection by the instrument as well as the HOM definition and the volatility classification. Moreover, the representation of the nucleation rates as a function of the total concentrations, not volume mixing ratios, removes the influence of the pressure effects on the molecule and cluster collision rates at different atmospheric altitudes.

Higher precursor concentrations lead to an increase in supersaturated mass of the mixture and, thus, to an increased NPF rate. This can be seen from the positive slope of the power law fits (lines) from the neutral NPF rates (J_n) in Fig. 8c. The slopes are sensitive to the interplay between particle growth rates and wall loss rates, as well as to the molecular composition of the critical clusters (Ehrhart and Curtius, 2013). In addition to the poorly quantified effect of temperature on the operation of condensation particle counters, including the PSM (Wimmer et al., 2015), another point to consider is that the NPF rates under ion-free conditions, especially at warmer temperatures, are low. Due to very low particle concentrations in the chamber, the data are close to the lower detection limit of the measurable formation rates. Both factors lead to a higher uncertainty in the nucleation rate calculation (Dada et al., 2020).

While there is no significant change in the NPF rate from +25 to −10 °C, a sharp increase of up to 2 orders of magnitude in J_n occurs at lower temperatures. This nonlinear behavior of the nucleation rates with decreasing temperature can be explained by the increased stability of the neutral clusters against evaporation without any stabilizing agent (e.g., ions), along with the strong temperature shift in the volatility classes. At low temperatures, more products belong to the ULVOC range and the increased concentration of LVOCs may enhance nucleation and certainly growth (Fig. 7). Due to the strong reduction in volatility, first-order oxidation products (OVOCs) will also take part in the initial growth of nucleating clusters at much smaller cluster sizes, while their oxidation rate is much less affected by the temperature compared to the autoxidation rate.

HOMs have high electrical polarizability, so ions can stabilize the embryonic clusters, also leading to a higher collision rate with other HOMs. Figure 8d shows that ions (GCR conditions) enhance the NPF rates by up to 2 orders of magnitude or more compared to neutral conditions, depending on the precursor concentrations and temperature. At higher levels of AP^{T}_{oxrate}, the neutral and the ion-induced cluster formation rates eventually converge (horizontal gray line), as the ion-induced nucleation rate is limited by the total ion-production rate (~ 4.1 ion pairs cm^{-3} s^{-1}) resulting from the galactic cosmic ray intensities at ground level. This comparison shows that the neutral HOM clusters are relatively unstable and, especially at high temperatures, have significant evaporation rates, which demonstrates the strong sensitivity of the pure biogenic nucleation to environmental conditions and the concentration of ions (Kirkby et al., 2016). The oxidation rate (AP^{T}_{oxrate}) at which J_n and J_{gcr} converge, however, depends strongly on temperature. At −50 °C the neutral and GCR nucleation rates almost coincide over the range of experimental measurements, reflecting the increased stability of the neutral clusters at low temperatures. This strong temperature sensitivity leads to a high nucleation potential of biogenic molecular clusters especially in cold regions (i.e., convective updraft of monoterpenes to higher altitudes). While our experiments were carried out at ground-level pressure (~ 970 hPa), we expect that our concentration-based NPF rates also apply to the upper troposphere within their uncertainties. The size and number of heavy atoms in the nucleating clusters containing two ULVOCs allow for the efficient distribution of the cluster formation energy in the form of vibrational and rotational excitation within the cluster. Therefore, we do not anticipate a strong pressure dependence throughout the troposphere for biogenic nucleation involving HOMs.

However, there might be other factors affecting the NPF in the upper troposphere. These include the increased ionization capacity, the absolute humidity, the coagulation sink and the availability of condensable gases for particle growth. Also, some chemical reactions are pressure dependent, but compared to their temperature dependence this is mostly a minor effect. Moreover, we believe that most of the HOMs are likely produced in the vicinity of their precursor sources, due to their high reactivity with oxidants, and then transported to higher altitudes by convective updrafts (Williamson et al., 2019) or are produced by second-generation chemistry. However, this is speculative and needs to be investigated in future studies.

3.6 Influence of UV light on α-pinene oxidation and NPF

In addition to ozone, $OH^{\bullet}$ radicals oxidize α-pinene and form HOMs, albeit with a lower yield. The lower yield results from the inability of $OH^{\bullet}$ to break the six-carbon ring of the α-pinene molecule, resulting in steric hindrance of the subsequent $RO_2^{\bullet}$ isomerization (Ehn et al., 2014; Berndt et al., 2016; Kirkby et al., 2016). This results in a higher energy barrier for formation of the intermediate alkyl radicals ($RO^{\bullet}$) and thus slows down the H-shift rate, which reduces highly oxidized products with low volatilities.

Figure S4 presents a mass defect plot showing the change between the UV-on and UV-off conditions of the last two GCR stages of the run shown in Fig. 1. The elevated $OH^{\bullet}$ radical concentration induced by the UV light leads to products with a higher H/C ratio than found in dark ozonolysis experiments (Fig. S5). The initial reaction of $OH^{\bullet}$ radicals with α-pinene forms reactive $RO_2^{\bullet}$ intermediate radicals of the chemical notation $C_{10}H_{17}O^{\bullet}_{odd}$, which also undergo several autoxidation steps (Berndt et al., 2018a). The bimolecular termination of this propagation chain leads to more HOM monomers of the chemical formula $C_{10}H_{16,18}O_x$ and subsequently more HOM dimers of the type $C_{20}H_{32,34}O_x$ (red and green trace, Fig. S6d–e), while products of the type $C_{10}H_{14}O_x$ and $C_{20}H_{30}O_x$ are reduced (blue trace, Fig. S6d–e). We note that nitrate ionization may have a reduced charging efficiency for HOMs formed from $OH^{\bullet}$ oxidation compared with those from ozonolysis, suggesting a possible measurement bias (Berndt et al., 2016).

Increasing the $OH^{\bullet}$ concentration in α-pinene oxidation experiments not only alters the molecular structure of the initial $RO_2^{\bullet}$ radicals but also influences the lifetime of the $RO_2^{\bullet}$ radicals and the HOM yield. The increase in $OH^{\bullet}$ affects the $HO_x^{\bullet}$ cycle and may increase $HO_2^{\bullet}$ radicals. The $HO_2^{\bullet}$ radicals will react with intermediate $RO_2^{\bullet}$ radicals and terminate the autoxidation at an earlier stage, leading mainly to closed-shell products of the type $C_{10}H_{16}O_{2+2n}$. The $HO_2^{\bullet}$ radicals also compete with the $RO_2^{\bullet}$–$RO_2^{\bullet}$ cross-reaction and so reduce dimer formation. Another source of HOM monomers may also be the subsequent reaction of primary α-pinene oxidation products (e.g., pinanediol) with $OH^{\bullet}$ radicals (Schobesberger et al., 2013; Ye et al., 2018).

As a result, the nucleation rates can be significantly influenced by the $HO_x^{\bullet}$ relative to $RO_2^{\bullet}$ concentrations ($HO_2^{\bullet}/RO_2^{\bullet}$ ratio), especially at higher temperature where the dimerization may be the rate-limiting step of pure biogenic nucleation. Compared to the atmosphere, in chamber experiments the $HO_2^{\bullet}/RO_2^{\bullet}$ ratio is shifted in the direction of the $RO_2^{\bullet}$ radical (Molteni et al., 2019). The difference between dark conditions and UV illumination may therefore be less pronounced in our study than in the real atmosphere. Keeping this caveat in mind, no pronounced variation in the overall HOM yield between UV illumination and its absence can be seen in Fig. 4. Furthermore, no photochemical reaction (degradation) seems to affect the total HOM yield. In summary, Fig. 8 shows similar nucleation rates between dark ozonolysis and UV-illuminated conditions, as indicated by the orange-framed symbols.

4 Conclusions

Measurements made in the CERN CLOUD chamber with two mass spectrometers – one using nitrate chemical ionization and the other a complementary proton transfer reaction – have provided a comprehensive molecular understanding of NPF from α-pinene between -50 and 25 °C. Using the mass spectrometry measurements, we performed two-dimensional volatility basis set calculations and determined the volatility distributions at each temperature. While at high temperatures the HOM dimers appear to be crucial for nucleation, at lower temperatures the HOM monomers and less oxygenated products also contribute.

Unimolecular autoxidation is key to the formation of HOMs from biogenic precursors. Intramolecular isomerization reactions, including the H-atom shift that leads to increased oxygenation, are found to be very sensitive to temperature. We observe a continuous reduction in the oxidation level (O/C ratio) and yield of HOMs as the temperature decreases from 25 to -50 °C. However, despite the lower oxidation level and lower yield of HOMs, our measurements show that the reduction in volatility more than compensates and, consequently, that the nucleation rates increase at lower temperatures.

This study demonstrates that chemical ionization mass spectrometers can measure the elemental composition and distribution of biogenic molecules over a wide range of oxidation states (O/C ratio) and at temperatures as low as -50 °C. PTR and nitrate chemical ionization mass spectrometers are necessary in future field and aircraft campaigns to study these processes in the atmosphere. Our results underscore the potential importance of biogenic nucleation throughout pristine regions of the atmosphere and especially in cold upper tropospheric environments exposed to convective outflows.

Data availability. Data related to this article are available upon request to the corresponding authors.

Supplement. The supplement related to this article is available online at: https://doi.org/10.5194/acp-20-9183-2020-supplement.

Author contributions. MSim, LD, MH, WS, DS, LF, ACW, BR, AK, XH, JA, RB, ABa, ABe, FB, SBrä, LC, DC, BC, AD, JDu, IE, HF, CF, LG, HG, MG, JH, VH, CK, WK, HL, CPL, KL, ML, HM, HEM, GM, BM, UM, AOn, EP, TP, JP, MP, LLJQ, MPR, SScho, SSchu, JS, MSip, GS, YS, YJT, ART, MV, AV, RW, MW, DSW, YW, SKW, YW, CY, PY, QY, MZ, XZ, RCF, RV, PMW and JK contributed to the development of the CLOUD facility and analysis instruments. MSim, LD, MH, WS, DS, LF, ACW, BR, XH, JA, RB, ABa, PSB, LB, ABe, FB, SBrä, SBri, LC, AD, DCD, JDu, IE, HF, LG, HG, MG, JH, VH, CRH, CK, WK, HL, CPL, KL, ML, HEM, GM, RM, BM, UM, LN, WN, AOj, EP, JP, LLJQ, AR, MPR, SScha, SSchu, JS, GS, YS, CT, YJT, ART, MV, AV, RW, DSW, YW, SKW, YW, MX, CY, PY, MZ, PMW and JK collected the data. MSim, LD, MH, WS, LF, ACW, BR, LG, CK, GM, BM, SKW, PY and RV performed modeling and analyzed the data. MSim, LD, MH, WS, DS, LF, ACW, BR, AK, HG, BM, UM, TP, MPR, PY, UB, JDo, RCF, AH, MK, DRW, NMD, JK and JC were involved in the scientific discussion and interpretation of the results. MSim, LD, MH, WS, AK, AV, UB, JDo, RCF, NMD, JK and JC contributed to the writing and editing of the manuscript.

Competing interests. The authors declare that they have no conflict of interest.

Special issue statement. This article is part of the special issue "The CERN CLOUD experiment (ACP/AMT inter-journal SI)". It is not associated with a conference.

Acknowledgements. We thank Patrick Carrie, Louis-Philippe De Menezes, Jonathan Dumollard, Katja Ivanova, Francisco Josa, Timo Keber, Ilia Krasin, Robert Kristic, Abdelmajid Laassiri, Osman Maksumov, Frank Malkemper, Benjamin Marichy, Herve Martinati, Sergey Vitaljevich Mizin,

Robert Sitals, Albin Wasem, and Mats Wilhelmsson for their contributions to the experiment.

Financial support. This research has received funding from the German Federal Ministry of Education and Research, CLOUD-12 (01LK1222A) and CLOUD-16 (01LK1601A); the European Commission Seventh Framework Programme and European Union Horizon 2020 program (Marie Skłodowska Curie ITNs no. 316662 "CLOUD-TRAIN", no. 764991 "CLOUD-MOTION", MSCA-IF no. 656994 "nano-CAVa", and MC-COFUND grant no. 600377); the European Research Council (ERC; project nos. 692891 "DAMOCLES", 638703 "COALA", 616075 "NANO-DYNAMITE", 335478 "QAPPA", 742206 "ATM-GP", 714621 "GASPARCON"); the Swiss National Science Foundation (project nos. 20020_152907, 200020_172602, 20FI20_159851, 20FI20_172622); the Academy of Finland (Centre of Excellence no. 307331, projects 299574, 296628, 306853, 304013, 310682); the Finnish Funding Agency for Technology and Innovation; the Väisälä Foundation; the Nessling Foundation; the Austrian Science Fund (FWF; project no. J3951-N36, project no. P27295-N20); the Austrian Research Promotion Agency (FFG, project no. 846050); the Portuguese Foundation for Science and Technology (project no. CERN/FIS-COM/0014/2017); the Swedish Research Council Formas (project number 2015-749); Vetenskapsrådet (grant 2011-5120); the Presidium of the Russian Academy of Sciences and Russian Foundation for Basic Research (grants 08-02-91006-CERN, 12-02-91522-CERN); the US National Science Foundation (grant nos. AGS1136479, AGS1447056, AGS1439551, CHE1012293, AGS1649147, AGS1602086, AGS1801280, AGS1801329, AGS1801574 and AGS1801897); the Wallace Research Foundation; the US Department of Energy (grant DE-SC0014469); the NERC GASSP project NE/J024252/1m; the Royal Society (Wolfson Merit Award); the UK Natural Environment Research Council (grant no. NE/K015966/1); Dreyfus Award EP-11-117; the French National Research Agency through the PIA (Programme d'Investissement d'Avenir), the Regional Council Nord-Pas de Calais, and the European Funds for Regional Economic Development Labex-Cappa (grant no. ANR-11-LABX-0005-01).

Review statement. This paper was edited by Manish Shrivastava and reviewed by two anonymous referees.

References

Almeida, J., Schobesberger, S., Kürten, A., Ortega, I. K., Kupiainen-Määttä, O., Praplan, A. P., Adamov, A., Amorim, A., Bianchi, F., Breitenlechner, M., David, A., Dommen, J., Donahue, N. M., Downard, A., Dunne, E., Duplissy, J., Ehrhart, S., Flagan, R. C., Franchin, A., Guida, R., Hakala, J., Hansel, A., Heinritzi, M., Henschel, H., Jokinen, T., Junninen, H., Kajos, M., Kangasluoma, J., Keskinen, H., Kupc, A., Kurtén, T., Kvashin, A. N., Laaksonen, A., Lehtipalo, K., Leiminger, M., Leppä, J., Loukonen, V., Makhmutov, V., Mathot, S., McGrath, M. J., Nieminen, T., Olenius, T., Onnela, A., Petäjä, T., Riccobono, F., Riipinen, I., Rissanen, M., Rondo, L., Ruuskanen, T., Santos, F. D., Sarnela, N., Schallhart, S., Schnitzhofer, R., Seinfeld, J. H., Simon, M., Sipilä, M., Stozhkov, Y., Stratmann, F., Tomé, A., Tröstl, J., Tsagkogeorgas, G., Vaattovaara, P., Viisanen, Y., Virtanen, A., Vrtala, A., Wagner, P. E., Weingartner, E., Wex, H., Williamson, C., Wimmer, D., Ye, P., Yli-Juuti, T., Carslaw, K. S., Kulmala, M., Curtius, J., Baltensperger, U., Worsnop, D. R., Vehkamäki, H., and Kirkby, J.: Molecular understanding of sulphuric acid–amine particle nucleation in the atmosphere, Nature, 502, 359–363, https://doi.org/10.1038/nature12663, 2013.

Ball, S. M., Hanson, D. R., Eisele, F. L., and McMurry, P. H.: Laboratory studies of particle nucleation: Initial results for H_2SO_4, H_2O, and NH_3 vapors, J. Geophys. Res.-Atmos., 104, 23709–23718, 1999.

Berndt, T., Richters, S., Kaethner, R., Voigtländer, J., Stratmann, F., Sipilä, M., Kulmala, M., and Herrmann, H.: Gas-Phase Ozonolysis of Cycloalkenes: Formation of Highly Oxidized RO_2 Radicals and Their Reactions with NO, NO_2, SO_2, and Other RO_2 Radicals, J. Phys. Chem. A, 119, 10336–10348, 2015.

Berndt, T., Richters, S., Jokinen, T., Hyttinen, N., Kurtén, T., Otkjær, R. V., Kjaergaard, H. G., Stratmann, F., Herrmann, H., Sipilä, M., Kulmala, M., and Ehn, M.: Hydroxyl radical-induced formation of highly oxidized organic compounds, Nat. Commun., 7, 13677, https://doi.org/10.1038/ncomms13677, 2016.

Berndt, T., Mentler, B., Scholz, W., Fischer, L., Herrmann, H., Kulmala, M., and Hansel, A.: Accretion Product Formation from Ozonolysis and OH Radical Reaction of α-Pinene: Mechanistic Insight and the Influence of Isoprene and Ethylene, Environ. Sci. Technol., 52, 11069–11077, https://doi.org/10.1021/acs.est.8b02210, 2018a.

Berndt, T., Scholz, W., Mentler, B., Fischer, L., Herrmann, H., Kulmala, M., and Hansel, A.: Accretion Product Formation from Self- and Cross-Reactions of RO_2 Radicals in the Atmosphere, Angew. Chem. Int. Edit., 57, 3820–3824, 2018b.

Bernhammer, A.-K., Breitenlechner, M., Keutsch, F. N., and Hansel, A.: Technical note: Conversion of isoprene hydroxy hydroperoxides (ISOPOOHs) on metal environmental simulation chamber walls, Atmos. Chem. Phys., 17, 4053–4062, https://doi.org/10.5194/acp-17-4053-2017, 2017.

Bianchi, F., Tröstl, J., Junninen, H., Frege, C., Henne, S., Hoyle, C. R., Molteni, U., Herrmann, E., Adamov, A., and Bukowiecki, N.: New particle formation in the free troposphere: A question of chemistry and timing, Science, 352, 1109–1112, 2016.

Bianchi, F., Garmash, O., He, X., Yan, C., Iyer, S., Rosendahl, I., Xu, Z., Rissanen, M. P., Riva, M., Taipale, R., Sarnela, N., Petäjä, T., Worsnop, D. R., Kulmala, M., Ehn, M., and Junninen, H.: The role of highly oxygenated molecules (HOMs) in determining the composition of ambient ions in the boreal forest, Atmos. Chem. Phys., 17, 13819–13831, https://doi.org/10.5194/acp-17-13819-2017, 2017

Bianchi, F., Kurtén, T., Riva, M., Mohr, C., Rissanen, M. P., Roldin, P., Berndt, T., Crounse, J. D., Wennberg, P. O., and Mentel, T. F.: Highly oxygenated organic molecules (HOM) from gas-phase autoxidation involving peroxy radicals: A key contributor to atmospheric aerosol, Chem. Rev., 119, 3472–3509, 2019.

Breitenlechner, M., Fischer, L., Hainer, M., Heinritzi, M., Curtius, J., and Hansel, A.: PTR3: An Instrument for Studying the Lifecycle of Reactive Organic Carbon in the Atmosphere, Anal. Chem., 89, 5824–5831, 2017.

Chew, A. A. and Atkinson, R.: OH radical formation yields from the gas-phase reactions of O_3 with alkenes and monoterpenes, J. Geophys. Res.-Atmos., 101, 28649–28653, 1996.

Crounse, J. D., Nielsen, L. B., Jørgensen, S., Kjaergaard, H. G., and Wennberg, P. O.: Autoxidation of Organic Compounds in the Atmosphere, J. Phys. Chem. Lett., 4, 3513–3520, 2013.

Dada, L., Lehtipalo, K., Kontkanen, J., Nieminen, T., Baalbaki, R., Ahonen, L., Duplissy, J., Yan, C., Chu, B., Petäjä, T., Lehtinen, K., Kerminen, V.-M., Kulmala, M., and Kangasluoma, J.: Formation and growth of sub-3-nm aerosol particles in experimental chambers, Nat. Protoc., 15, 1013–1040, 2020.

Dias, A., Ehrhart, S., Vogel, A., Williamson, C., Almeida, J., Kirkby, J., Mathot, S., Mumford, S., and Onnela, A.: Temperature uniformity in the CERN CLOUD chamber, Atmos. Meas. Tech., 10, 5075–5088, https://doi.org/10.5194/amt-10-5075-2017, 2017.

Donahue, N. M., Epstein, S. A., Pandis, S. N., and Robinson, A. L.: A two-dimensional volatility basis set: 1. organic-aerosol mixing thermodynamics, Atmos. Chem. Phys., 11, 3303–3318, https://doi.org/10.5194/acp-11-3303-2011, 2011.

Donahue, N. M., Kroll, J. H., Pandis, S. N., and Robinson, A. L.: A two-dimensional volatility basis set – Part 2: Diagnostics of organic-aerosol evolution, Atmos. Chem. Phys., 12, 615–634, https://doi.org/10.5194/acp-12-615-2012, 2012.

Donahue, N. M., Ortega, I. K., Chuang, W., Riipinen, I., Riccobono, F., Schobesberger, S., Dommen, J., Baltensperger, U., Kulmala, M., and Worsnop, D. R.: How do organic vapors contribute to new-particle formation?, Faraday Discuss., 165, 91–104, 2013.

Duplissy, J., Merikanto, J., Franchin, A., Tsagkogeorgas, G., Kangasluoma, J., Wimmer, D., Vuollekoski, H., Schobesberger, S., Lehtipalo, K., Flagan, R. C., Brus, D., Donahue, N. M., Vehkamäki, H., Almeida, J., Amorim, A., Barmet, P., Bianchi, F., Breitenlechner, M., Dunne, E. M., Guida, R., Henschel, H., Junninen, H., Kirkby, J., Kürten, A., Kupc, A., Määttänen, A., Makhmutov, V., Mathot, S., Nieminen, T., Onnela, A., Praplan, A. P., Riccobono, F., Rondo, L., Steiner, G., Tome, A., Walther, H., Baltensperger, U., Carslaw, K. S., Dommen, J., Hansel, A., Petäjä, T., Sipilä, M., Stratmann, F., Vrtala, A., Wagner, P. E., Worsnop, D. R., Curtius, J., and Kulmala, M.: Effect of ions on sulfuric acid-water binary particle formation: 2. Experimental data and comparison with QC-normalized classical nucleation theory, J. Geophys. Res.-Atmos., 121, 1752–1775, 2016.

Dusek, U., Frank, G., Hildebrandt, L., Curtius, J., Schneider, J., Walter, S., Chand, D., Drewnick, F., Hings, S., and Jung, D.: Size matters more than chemistry for cloud-nucleating ability of aerosol particles, Science, 312, 1375–1378, 2006.

Ehn, M., Thornton, J. A., Kleist, E., Sipila, M., Junninen, H., Pullinen, I., Springer, M., Rubach, F., Tillmann, R., Lee, B., Lopez-Hilfiker, F., Andres, S., Acir, I.-H., Rissanen, M., Jokinen, T., Schobesberger, S., Kangasluoma, J., Kontkanen, J., Nieminen, T., Kurten, T., Nielsen, L. B., Jorgensen, S., Kjaergaard, H. G., Canagaratna, M., Maso, M. D., Berndt, T., Petaja, T., Wahner, A., Kerminen, V.-M., Kulmala, M., Worsnop, D. R., Wildt, J., and Mentel, T. F.: A large source of low-volatility secondary organic aerosol, Nature, 506, 476–479, 2014.

Ehn, M., Berndt, T., Wildt, J., and Mentel, T.: Highly Oxygenated Molecules from Atmospheric Autoxidation of Hydrocarbons: A Prominent Challenge for Chemical Kinetics Studies, Int. J. Chem. Kinet., 49, 821–831, 2017.

Ehrhart, S. and Curtius, J.: Influence of aerosol lifetime on the interpretation of nucleation experiments with respect to the first nucleation theorem, Atmos. Chem. Phys., 13, 11465–11471, https://doi.org/10.5194/acp-13-11465-2013, 2013.

Eisele, F. and Tanner, D.: Measurement of the gas phase concentration of H_2SO_4 and methane sulfonic acid and estimates of H_2SO_4 production and loss in the atmosphere, J. Geophys. Res.-Atmos., 98, 9001–9010, 1993.

Epstein, S. A., Riipinen, I., and Donahue, N. M.: A semiempirical correlation between enthalpy of vaporization and saturation concentration for organic aerosol, Environ. Sci. Technol., 44, 743–748, 2009.

Frege, C., Ortega, I. K., Rissanen, M. P., Praplan, A. P., Steiner, G., Heinritzi, M., Ahonen, L., Amorim, A., Bernhammer, A.-K., Bianchi, F., Brilke, S., Breitenlechner, M., Dada, L., Dias, A., Duplissy, J., Ehrhart, S., El-Haddad, I., Fischer, L., Fuchs, C., Garmash, O., Gonin, M., Hansel, A., Hoyle, C. R., Jokinen, T., Junninen, H., Kirkby, J., Kürten, A., Lehtipalo, K., Leiminger, M., Mauldin, R. L., Molteni, U., Nichman, L., Petäjä, T., Sarnela, N., Schobesberger, S., Simon, M., Sipilä, M., Stolzenburg, D., Tomé, A., Vogel, A. L., Wagner, A. C., Wagner, R., Xiao, M., Yan, C., Ye, P., Curtius, J., Donahue, N. M., Flagan, R. C., Kulmala, M., Worsnop, D. R., Winkler, P. M., Dommen, J., and Baltensperger, U.: Influence of temperature on the molecular composition of ions and charged clusters during pure biogenic nucleation, Atmos. Chem. Phys., 18, 65–79, https://doi.org/10.5194/acp-18-65-2018, 2018.

Fu, Y., Xue, M., Cai, R., Kangasluoma, J., and Jiang, J.: Theoretical and experimental analysis of the core sampling method: Reducing diffusional losses in aerosol sampling line, Aerosol Sci. Tech., 53, 793–801, 2019.

Gordon, H., Kirkby, J., Baltensperger, U., Bianchi, F., Breitenlechner, M., Curtius, J., Dias, A., Dommen, J., Donahue, N. M., and Dunne, E. M.: Causes and importance of new particle formation in the present-day and preindustrial atmospheres, J. Geophys. Res.-Atmos., 122, 8739–8760, https://doi.org/10.1002/2017JD026844, 2017.

Hallquist, M., Wenger, J. C., Baltensperger, U., Rudich, Y., Simpson, D., Claeys, M., Dommen, J., Donahue, N. M., George, C., Goldstein, A. H., Hamilton, J. F., Herrmann, H., Hoffmann, T., Iinuma, Y., Jang, M., Jenkin, M. E., Jimenez, J. L., Kiendler-Scharr, A., Maenhaut, W., McFiggans, G., Mentel, Th. F., Monod, A., Prévôt, A. S. H., Seinfeld, J. H., Surratt, J. D., Szmigielski, R., and Wildt, J.: The formation, properties and impact of secondary organic aerosol: current and emerging issues, Atmos. Chem. Phys., 9, 5155–5236, https://doi.org/10.5194/acp-9-5155-2009, 2009.

Hanson, D. and Eisele, F.: Diffusion of H_2SO_4 in humidified nitrogen: Hydrated H_2SO_4, J. Phys. Chem. A, 104, 1715–1719, 2000.

Heinritzi, M., Simon, M., Steiner, G., Wagner, A. C., Kürten, A., Hansel, A., and Curtius, J.: Characterization of the mass-dependent transmission efficiency of a CIMS, Atmos. Meas. Tech., 9, 1449–1460, https://doi.org/10.5194/amt-9-1449-2016, 2016.

Hyttinen, N., Kupiainen-Määttä, O., Rissanen, M. P., Muuronen, M., Ehn, M., and Kurtén, T.: Modeling the charging of highly oxidized cyclohexene ozonolysis products using nitrate-based chemical ionization, J. Phys. Chem. A, 119, 6339–6345, 2015.

Hyttinen, N., Rissanen, M. P., and Kurtén, T.: Computational Comparison of Acetate and Nitrate Chemical Ionization of Highly Oxidized Cyclohexene Ozonolysis Intermediates and Products, J. Phys. Chem. A, 121, 2172–2179, 2017.

Jimenez, J. L., Canagaratna, M., Donahue, N., Prevot, A., Zhang, Q., Kroll, J. H., DeCarlo, P. F., Allan, J. D., Coe, H., and Ng, N.: Evolution of organic aerosols in the atmosphere, Science, 326, 1525–1529, 2009.

Jokinen, T., Berndt, T., Makkonen, R., Kerminen, V.-M., Junninen, H., Paasonen, P., Stratmann, F., Herrmann, H., Guenther, A. B., and Worsnop, D. R.: Production of extremely low volatile organic compounds from biogenic emissions: Measured yields and atmospheric implications, P. Natl. Acad. Sci. USA, 112, 7123–7128, 2015.

Jokinen, T., Sipilä, M., Junninen, H., Ehn, M., Lönn, G., Hakala, J., Petäjä, T., Mauldin III, R. L., Kulmala, M., and Worsnop, D. R.: Atmospheric sulphuric acid and neutral cluster measurements using CI-APi-TOF, Atmos. Chem. Phys., 12, 4117–4125, https://doi.org/10.5194/acp-12-4117-2012, 2012.

Kerminen, V.-M., Chen, X., Vakkari, V., Petäjä, T., Kulmala, M., and Bianchi, F.: Atmospheric new particle formation and growth: review of field observations, Environ. Res. Lett., 13, 103003, https://doi.org/10.1088/1748-9326/aadf3c, 2018.

Kirkby, J., Curtius, J., Almeida, J., Dunne, E., Duplissy, J., Ehrhart, S., Franchin, A., Gagné, S., Ickes, L., Kürten, A., Kupc, A., Metzger, A., Riccobono, F., Rondo, L., Schobesberger, S., Tsagkogeorgas, G., Wimmer, D., Amorim, A., Bianchi, F., Breitenlechner, M., David, A., Dommen, J., Downard, A., Ehn, M., Flagan, R. C., Haider, S., Hansel, A., Hauser, D., Jud, W., Junninen, H., Kreissl, F., Kvashin, A., Laaksonen, A., Lehtipalo, K., Lima, J., Lovejoy, E. R., Makhmutov, V., Mathot, S., Mikkilä, J., Minginette, P., Mogo, S., Nieminen, T., Onnela, A., Pereira, P., Petäjä, T., Schnitzhofer, R., Seinfeld, J. H., Sipilä, M., Stozhkov, Y., Stratmann, F., Tomé, A., Vanhanen, J., Viisanen, Y., Vrtala, A., Wagner, P. E., Walther, H., Weingartner, E., Wex, H., Winkler, P. M., Carslaw, K. S., Worsnop, D. R., Baltensperger, U., and Kulmala, M.: Role of sulphuric acid, ammonia and galactic cosmic rays in atmospheric aerosol nucleation, Nature, 476, 429, https://doi.org/10.1038/nature10343, 2011.

Kirkby, J., Duplissy, J., Sengupta, K., Frege, C., Gordon, H., Williamson, C., Heinritzi, M., Simon, M., Yan, C., Almeida, J., Tröstl, J., Nieminen, T., Ortega, I. K., Wagner, R., Adamov, A., Amorim, A., Bernhammer, A.-K., Bianchi, F., Breitenlechner, M., Brilke, S., Chen, X., Craven, J., Dias, A., Ehrhart, S., Flagan, R. C., Franchin, A., Fuchs, C., Guida, R., Hakala, J., Hoyle, C. R., Jokinen, T., Junninen, H., Kangasluoma, J., Kim, J., Krapf, M., Kürten, A., Laaksonen, A., Lehtipalo, K., Makhmutov, V., Mathot, S., Molteni, U., Onnela, A., Peräkylä, O., Piel, F., Petäjä, T., Praplan, A. P., Pringle, K., Rap, A., Richards, N. A. D., Riipinen, I., Rissanen, M. P., Rondo, L., Sarnela, N., Schobesberger, S., Scott, C. E., Seinfeld, J. H., Sipilä, M., Steiner, G., Stozhkov, Y., Stratmann, F., Tomé, A., Virtanen, A., Vogel, A. L., Wagner, A. C., Wagner, P. E., Weingartner, E., Wimmer, D., Winkler, P. M., Ye, P., Zhang, X., Hansel, A., Dommen, J., Donahue, N. M., Worsnop, D. R., Baltensperger, U., Kulmala, M., Carslaw, K. S., and Curtius, J.: Ion-induced nucleation of pure biogenic particles, Nature, 533, 521–526, 2016.

Knopf, D. A., Pöschl, U., and Shiraiwa, M.: Radial diffusion and penetration of gas molecules and aerosol particles through laminar flow reactors, denuders, and sampling tubes, Anal. Chem., 87, 3746–3754, 2015.

Kristensen, K., Jensen, L., Glasius, M., and Bilde, M.: The effect of sub-zero temperature on the formation and composition of secondary organic aerosol from ozonolysis of alpha-pinene, Environ. Sci.-Proc. Imp., 19, 1220–1234, 2017.

Kuang, C., McMurry, P. H., McCormick, A. V., and Eisele, F. L.: Dependence of nucleation rates on sulfuric acid vapor concentration in diverse atmospheric locations, J. Geophys. Res.-Atmos., 113, D10209, https://doi.org/10.1029/2007JD009253, 2008.

Kulmala, M., Vehkamäki, H., Petäjä, T., Dal Maso, M., Lauri, A., Kerminen, V. M., Birmili, W., and McMurry, P. H.: Formation and growth rates of ultrafine atmospheric particles: a review of observations, J. Aerosol Sci., 35, 143–176, 2004.

Kulmala, M., Kontkanen, J., Junninen, H., Lehtipalo, K., Manninen, H. E., Nieminen, T., Petaja, T., Sipila, M., Schobesberger, S., Rantala, P., Franchin, A., Jokinen, T., Jarvinen, E., Aijala, M., Kangasluoma, J., Hakala, J., Aalto, P. P., Paasonen, P., Mikkila, J., Vanhanen, J., Aalto, J., Hakola, H., Makkonen, U., Ruuskanen, T., Mauldin, R. L., Duplissy, J., Vehkamaki, H., Back, J., Kortelainen, A., Riipinen, I., Kurten, T., Johnston, M. V., Smith, J. N., Ehn, M., Mentel, T. F., Lehtinen, K. E. J., Laaksonen, A., Kerminen, V. M., and Worsnop, D. R.: Direct Observations of Atmospheric Aerosol Nucleation, Science, 339, 943–946, 2013.

Kupc, A., Amorim, A., Curtius, J., Danielczok, A., Duplissy, J., Ehrhart, S., Walther, H., Ickes, L., Kirkby, J., and Kürten, A.: A fibre-optic UV system for H_2SO_4 production in aerosol chambers causing minimal thermal effects, J. Aerosol Sci., 42, 532–543, 2011.

Kürten, A., Rondo, L., Ehrhart, S., and Curtius, J.: Performance of a corona ion source for measurement of sulfuric acid by chemical ionization mass spectrometry, Atmos. Meas. Tech., 4, 437–443, https://doi.org/10.5194/amt-4-437-2011, 2011.

Kürten, A., Rondo, L., Ehrhart, S., and Curtius, J.: Calibration of a Chemical Ionization Mass Spectrometer for the Measurement of Gaseous Sulfuric Acid, J. Phys. Chem. A, 116, 6375–6386, 2012.

Kürten, A., Jokinen, T., Simon, M., Sipilä, M., Sarnela, N., Junninen, H., Adamov, A., Almeida, J., Amorim, A., Bianchi, F., Breitenlechner, M., Dommen, J., Donahue, N. M., Duplissy, J., Ehrhart, S., Flagan, R. C., Franchin, A., Hakala, J., Hansel, A., Heinritzi, M., Hutterli, M., Kangasluoma, J., Kirkby, J., Laaksonen, A., Lehtipalo, K., Leiminger, M., Makhmutov, V., Mathot, S., Onnela, A., Petäjä, T., Praplan, A. P., Riccobono, F., Rissanen, M. P., Rondo, L., Schobesberger, S., Seinfeld, J. H., Steiner, G., Tomé, A., Tröstl, J., Winkler, P. M., Williamson, C., Wimmer, D., Ye, P., Baltensperger, U., Carslaw, K. S., Kulmala, M., Worsnop, D. R., and Curtius, J.: Neutral molecular cluster formation of sulfuric acid–dimethylamine observed in real time under atmospheric conditions, P. Natl. Acad. Sci. USA, 111, 15019–15024, 2014.

Kürten, A., Williamson, C., Almeida, J., Kirkby, J., and Curtius, J.: On the derivation of particle nucleation rates from experimental formation rates, Atmos. Chem. Phys., 15, 4063–4075, https://doi.org/10.5194/acp-15-4063-2015, 2015.

Kürten, A., Bianchi, F., Almeida, J., Kupiainen-Määttä, O., Dunne, E. M., Duplissy, J., Williamson, C., Barmet, P., Breitenlechner, M., and Dommen, J.: Experimental particle formation rates spanning tropospheric sulfuric acid and ammonia abundances, ion

production rates, and temperatures, J. Geophys. Res.-Atmos., 121, 12377–12400, 2016.

Kurtén, T., Loukonen, V., Vehkamäki, H., and Kulmala, M.: Amines are likely to enhance neutral and ion-induced sulfuric acid-water nucleation in the atmosphere more effectively than ammonia, Atmos. Chem. Phys., 8, 4095–4103, https://doi.org/10.5194/acp-8-4095-2008, 2008.

Kurtén, T., Rissanen, M. P., Mackeprang, K., Thornton, J. A., Hyttinen, N., Jørgensen, S., Ehn, M., and Kjaergaard, H. G.: Computational study of hydrogen shifts and ring-opening mechanisms in α-pinene ozonolysis products, J. Phys. Chem. A, 119, 11366–11375, 2015.

Kurtén, T., Tiusanen, K., Roldin, P., Rissanen, M., Luy, J.-N., Boy, M., Ehn, M., and Donahue, N.: α-Pinene Autoxidation Products May Not Have Extremely Low Saturation Vapor Pressures Despite High O : C Ratios, J. Phys. Chem. A, 120, 2569–2582, 2016.

Lehtipalo, K., Leppä, J., Kontkanen, J., Kangasluoma, J., Franchin, A., Wimmer, D., Schobesberger, S., Junninen, H., Petäjä, T., Sipilä, M., Mikkilä, J., Vanhanen, J., Worsnop, D. R., and Kulmala, M.: Methods for determining particle size distribution and growth rates between 1 and 3 nm using the Particle Size Magnifier, Boreal Environ. Res., 19, 215–236, 2014.

Lehtipalo, K., Yan, C., Dada, L., Bianchi, F., Xiao, M., Wagner, R., Stolzenburg, D., Ahonen, L. R., Amorim, A., and Baccarini, A.: Multicomponent new particle formation from sulfuric acid, ammonia, and biogenic vapors, Sci. Adv., 4, eaau5363, https://doi.org/10.1126/sciadv.aau5363, 2018.

Lopez-Hilfiker, F. D., Mohr, C., Ehn, M., Rubach, F., Kleist, E., Wildt, J., Mentel, Th. F., Lutz, A., Hallquist, M., Worsnop, D., and Thornton, J. A.: A novel method for online analysis of gas and particle composition: description and evaluation of a Filter Inlet for Gases and AEROsols (FIGAERO), Atmos. Meas. Tech., 7, 983–1001, https://doi.org/10.5194/amt-7-983-2014, 2014.

Manninen, H. E., Petäjä, T., Asmi, E., Riipinen, I., Nieminen, T., Mikkilä, J., Hõrrak, U., Mirme, A., Mirme, S., and Laakso, L.: Long-term field measurements of charged and neutral clusters using Neutral cluster and Air Ion Spectrometer (NAIS), Boreal Environ. Res., 14, 591–605, 2009.

Merikanto, J., Spracklen, D. V., Mann, G. W., Pickering, S. J., and Carslaw, K. S.: Impact of nucleation on global CCN, Atmos. Chem. Phys., 9, 8601–8616, https://doi.org/10.5194/acp-9-8601-2009, 2009.

Mohr, C., Lopez-Hilfiker, F. D., Yli-Juuti, T., Heitto, A., Lutz, A., Hallquist, M., D'Ambro, E. L., Rissanen, M. P., Hao, L., and Schobesberger, S.: Ambient observations of dimers from terpene oxidation in the gas phase: Implications for new particle formation and growth, Geophys. Res. Lett., 44, 2958–2966, 2017.

Molteni, U., Simon, M., Heinritzi, M., Hoyle, C. R., Bernhammer, A.-K., Bianchi, F., Breitenlechner, M., Brilke, S., Dias, A., and Duplissy, J.: Formation of Highly Oxygenated Organic Molecules from alpha-Pinene Ozonolysis, ACS Earth Space Chem., 3, 873–883 https://doi.org/10.1021/acsearthspacechem.9b00035, 2019.

Ng, N. L., Chhabra, P. S., Chan, A. W. H., Surratt, J. D., Kroll, J. H., Kwan, A. J., McCabe, D. C., Wennberg, P. O., Sorooshian, A., Murphy, S. M., Dalleska, N. F., Flagan, R. C., and Seinfeld, J. H.: Effect of NO_x level on secondary organic aerosol (SOA) formation from the photooxidation of terpenes, Atmos. Chem. Phys., 7, 5159–5174, https://doi.org/10.5194/acp-7-5159-2007, 2007.

O'Dowd, C. D., Jimenez, J. L., Bahreini, R., Flagan, R. C., Seinfeld, J. H., Hämeri, K., Pirjola, L., Kulmala, M., Jennings, S. G., and Hoffmann, T.: Marine aerosol formation from biogenic iodine emissions, Nature, 417, 632–636, https://doi.org/10.1038/nature00775, 2002.

Pankow, J. F. and Asher, W. E.: SIMPOL.1: a simple group contribution method for predicting vapor pressures and enthalpies of vaporization of multifunctional organic compounds, Atmos. Chem. Phys., 8, 2773–2796, https://doi.org/10.5194/acp-8-2773-2008, 2008.

Passananti, M., Zapadinsky, E., Zanca, T., Kangasluoma, J., Myllys, N., Rissanen, M. P., Kurtén, T., Ehn, M., Attoui, M., and Vehkamäki, H.: How well can we predict cluster fragmentation inside a mass spectrometer?, Chem. Commun., 55, 5946–5949, 2019.

Praske, E., Otkjær, R. V., Crounse, J. D., Hethcox, J. C., Stoltz, B. M., Kjaergaard, H. G., and Wennberg, P. O.: Atmospheric autoxidation is increasingly important in urban and suburban North America, P. Natl. Acad. Sci. USA, 115, 64–69, 2018.

Presto, A. A., Huff Hartz, K. E., and Donahue, N. M.: Secondary organic aerosol production from terpene ozonolysis. 2. Effect of NO_x concentration, Environ. Sci. Technol., 39, 7046–7054, 2005.

Quéléver, L. L. J., Kristensen, K., Normann Jensen, L., Rosati, B., Teiwes, R., Daellenbach, K. R., Peräkylä, O., Roldin, P., Bossi, R., Pedersen, H. B., Glasius, M., Bilde, M., and Ehn, M.: Effect of temperature on the formation of highly oxygenated organic molecules (HOMs) from alpha-pinene ozonolysis, Atmos. Chem. Phys., 19, 7609–7625, https://doi.org/10.5194/acp-19-7609-2019, 2019.

Riccobono, F., Schobesberger, S., Scott, C. E., Dommen, J., Ortega, I. K., Rondo, L., Almeida, J., Amorim, A., Bianchi, F., Breitenlechner, M., David, A., Downard, A., Dunne, E. M., Duplissy, J., Ehrhart, S., Flagan, R. C., Franchin, A., Hansel, A., Junninen, H., Kajos, M., Keskinen, H., Kupc, A., Kürten, A., Kvashin, A. N., Laaksonen, A., Lehtipalo, K., Makhmutov, V., Mathot, S., Nieminen, T., Onnela, A., Petäjä, T., Praplan, A. P., Santos, F. D., Schallhart, S., Seinfeld, J. H., Sipilä, M., Spracklen, D. V., Stozhkov, Y., Stratmann, F., Tomé, A., Tsagkogeorgas, G., Vaattovaara, P., Viisanen, Y., Vrtala, A., Wagner, P. E., Weingartner, E., Wex, H., Wimmer, D., Carslaw, K. S., Curtius, J., Donahue, N. M., Kirkby, J., Kulmala, M., Worsnop, D. R., and Baltensperger, U.: Oxidation Products of Biogenic Emissions Contribute to Nucleation of Atmospheric Particles, Science, 344, 717–721, https://doi.org/10.1126/science.1243527, 2014.

Riipinen, I., Yli-Juuti, T., Pierce, J. R., Petäjä, T., Worsnop, D. R., Kulmala, M., and Donahue, N. M.: The contribution of organics to atmospheric nanoparticle growth, Nat. Geosci., 5, 453–458, 2012.

Rissanen, M. P.: NO_2 Suppression of Autoxidation–Inhibition of Gas-Phase Highly Oxidized Dimer Product Formation, ACS Earth Space Chem., 2, 1211–1219, 2018.

Rissanen, M. P., Kurtén, T., Sipilä, M., Thornton, J. A., Kangasluoma, J., Sarnela, N., Junninen, H., Jørgensen, S., Schallhart, S., and Kajos, M. K.: The formation of highly oxidized multifunctional products in the ozonolysis of cyclohexene, J. Am. Chem. Soc., 136, 15596–15606, 2014.

Rissanen, M. P., Kurtén, T., Sipilä, M., Thornton, J. A., Kausiala, O., Garmash, O., Kjaergaard, H. G., Petäjä, T., Worsnop, D. R., Ehn, M., and Kulmala, M.: Effects of Chemical Complexity on the Autoxidation Mechanisms of Endocyclic Alkene Ozonolysis Products: From Methylcyclohexenes toward Understanding α-Pinene, J. Phys. Chem. A, 119, 4633–4650, 2015.

Saathoff, H., Naumann, K.-H., Möhler, O., Jonsson, Å. M., Hallquist, M., Kiendler-Scharr, A., Mentel, Th. F., Tillmann, R., and Schurath, U.: Temperature dependence of yields of secondary organic aerosols from the ozonolysis of α-pinene and limonene, Atmos. Chem. Phys., 9, 1551–1577, https://doi.org/10.5194/acp-9-1551-2009, 2009.

Schervish, M. and Donahue, N. M.: Peroxy radical chemistry and the volatility basis set, Atmos. Chem. Phys., 20, 1183–1199, https://doi.org/10.5194/acp-20-1183-2020, 2020.

Schnitzhofer, R., Metzger, A., Breitenlechner, M., Jud, W., Heinritzi, M., De Menezes, L.-P., Duplissy, J., Guida, R., Haider, S., Kirkby, J., Mathot, S., Minginette, P., Onnela, A., Walther, H., Wasem, A., Hansel, A., and the CLOUD Team: Characterisation of organic contaminants in the CLOUD chamber at CERN, Atmos. Meas. Tech., 7, 2159–2168, https://doi.org/10.5194/amt-7-2159-2014, 2014.

Schobesberger, S., D'Ambro, E. L., Lopez-Hilfiker, F. D., Mohr, C., and Thornton, J. A.: A model framework to retrieve thermodynamic and kinetic properties of organic aerosol from composition-resolved thermal desorption measurements, Atmos. Chem. Phys., 18, 14757–14785, https://doi.org/10.5194/acp-18-14757-2018, 2018.

Schobesberger, S., Junninen, H., Bianchi, F., Lönn, G., Ehn, M., Lehtipalo, K., Dommen, J., Ehrhart, S., Ortega, I. K., Franchin, A., Nieminen, T., Riccobono, F., Hutterli, M., Duplissy, J., Almeida, J., Amorim, A., Breitenlechner, M., Downard, A. J., Dunne, E. M., Flagan, R. C., Kajos, M., Keskinen, H., Kirkby, J., Kupc, A., Kürten, A., Kurtén, T., Laaksonen, A., Mathot, S., Onnela, A., Praplan, A. P., Rondo, L., Santos, F. D., Schallhart, S., Schnitzhofer, R., Sipilä, M., Tomé, A., Tsagkogeorgas, G., Vehkamäki, H., Wimmer, D., Baltensperger, U., Carslaw, K. S., Curtius, J., Hansel, A., Petäjä, T., Kulmala, M., Donahue, N. M., and Worsnop, D. R.: Molecular understanding of atmospheric particle formation from sulfuric acid and large oxidized organic molecules, P. Natl. Acad. Sci. USA, 110, 17223–17228, 2013.

Simon, M., Heinritzi, M., Herzog, S., Leiminger, M., Bianchi, F., Praplan, A., Dommen, J., Curtius, J., and Kürten, A.: Detection of dimethylamine in the low pptv range using nitrate chemical ionization atmospheric pressure interface time-of-flight (CI-APi-TOF) mass spectrometry, Atmos. Meas. Tech., 9, 2135–2145, https://doi.org/10.5194/amt-9-2135-2016, 2016.

Sindelarova, K., Granier, C., Bouarar, I., Guenther, A., Tilmes, S., Stavrakou, T., Müller, J.-F., Kuhn, U., Stefani, P., and Knorr, W.: Global data set of biogenic VOC emissions calculated by the MEGAN model over the last 30 years, Atmos. Chem. Phys., 14, 9317–9341, https://doi.org/10.5194/acp-14-9317-2014, 2014.

Sipilä, M., Sarnela, N., Jokinen, T., Henschel, H., Junninen, H., Kontkanen, J., Richters, S., Kangasluoma, J., Franchin, A., Peräkylä, O., Rissanen, M. P., Ehn, M., Vehkamäki, H., Kurten, T., Berndt, T., Petäjä, T., Worsnop, D., Ceburnis, D., Kerminen, V.-M., Kulmala, M., and O'Dowd, C.: Molecular-scale evidence of aerosol particle formation via sequential addition of HIO3, Nature, 537, 532–534, https://doi.org/10.1038/nature19314, 2016.

Spracklen, D. V., Carslaw, K. S., Kulmala, M., Kerminen, V. M., Sihto, S. L., Riipinen, I., Merikanto, J., Mann, G. W., Chipperfield, M. P., and Wiedensohler, A.: Contribution of particle formation to global cloud condensation nuclei concentrations, Geophys. Res. Lett., 35, L06808, https://doi.org/10.1029/2007GL033038, 2008.

IPCC: Climate Change 2013: The Physical Science Basis. Contribution of Working Group I to the Fifth Assessment Report of the Intergovernmental Panel on Climate Change, edited by: Stocker, T. F., Qin, D., Plattner, G.-K., Tignor, M., Allen, S. K., Boschung, J., Nauels, A., Xia, Y., Bex, V., and Midgley, P. M., Cambridge University Press, Cambridge, United Kingdom and New York, NY, USA, 1535 pp., 2013.

Stolzenburg, D., Steiner, G., and Winkler, P. M.: A DMA-train for precision measurement of sub-10 nm aerosol dynamics, Atmos. Meas. Tech., 10, 1639–1651, https://doi.org/10.5194/amt-10-1639-2017, 2017.

Stolzenburg, D., Fischer, L., Vogel, A. L., Heinritzi, M., Schervish, M., Simon, M., Wagner, A. C., Dada, L., Ahonen, L. R., and Amorim, A.: Rapid growth of organic aerosol nanoparticles over a wide tropospheric temperature range, P. Natl. Acad. Sci. USA, 115, 9122–9127, https://doi.org/10.1073/pnas.1807604115, 2018.

Tröstl, J., Chuang, W. K., Gordon, H., Heinritzi, M., Yan, C., Molteni, U., Ahlm, L., Frege, C., Bianchi, F., Wagner, R., Simon, M., Lehtipalo, K., Williamson, C., Craven, J. S., Duplissy, J., Adamov, A., Almeida, J., Bernhammer, A.-K., Breitenlechner, M., Brilke, S., Dias, A., Ehrhart, S., Flagan, R. C., Franchin, A., Fuchs, C., Guida, R., Gysel, M., Hansel, A., Hoyle, C. R., Jokinen, T., Junninen, H., Kangasluoma, J., Keskinen, H., Kim, J., Krapf, M., Kürten, A., Laaksonen, A., Lawler, M., Leiminger, M., Mathot, S., Möhler, O., Nieminen, T., Onnela, A., Petäjä, T., Piel, F. M., Miettinen, P., Rissanen, M. P., Rondo, L., Sarnela, N., Schobesberger, S., Sengupta, K., Sipilä, M., Smith, J. N., Steiner, G., Tomè, A., Virtanen, A., Wagner, A. C., Weingartner, E., Wimmer, D., Winkler, P. M., Ye, P., Carslaw, K. S., Curtius, J., Dommen, J., Kirkby, J., Kulmala, M., Riipinen, I., Worsnop, D. R., Donahue, N. M., and Baltensperger, U.: The role of low-volatility organic compounds in initial particle growth in the atmosphere, Nature, 533, 527–531, https://doi.org/10.1038/nature18271, 2016.

Valiev, R. R., Hasan, G., Salo, V.-T., Kubečka, J., and Kurten, T.: Intersystem Crossings Drive Atmospheric Gas-Phase Dimer Formation, J. Phys. Chem. A, 123, 6596–6604, 2019.

Vanhanen, J., Mikkilä, J., Lehtipalo, K., Sipilä, M., Manninen, H. E., Siivola, E., Petäjä, T., and Kulmala, M.: Particle Size Magnifier for Nano-CN Detection, Aerosol Sci. Tech., 45, 533–542, 2011.

Viggiano, A., Seeley, J. V., Mundis, P. L., Williamson, J. S., and Morris, R. A.: Rate Constants for the Reactions of $XO_3^-(H_2O)_n$ ($X = $ C, HC, and N) and $NO_3^-(HNO_3)_n$ with H_2SO_4: Implications for Atmospheric Detection of H_2SO_4, J. Phys. Chem. A, 101, 8275–8278, 1997.

Wagner, R., Yan, C., Lehtipalo, K., Duplissy, J., Nieminen, T., Kangasluoma, J., Ahonen, L. R., Dada, L., Kontkanen, J., Manninen, H. E., Dias, A., Amorim, A., Bauer, P. S., Bergen, A., Bernhammer, A.-K., Bianchi, F., Brilke, S., Mazon, S. B., Chen, X.,

Draper, D. C., Fischer, L., Frege, C., Fuchs, C., Garmash, O., Gordon, H., Hakala, J., Heikkinen, L., Heinritzi, M., Hofbauer, V., Hoyle, C. R., Kirkby, J., Kürten, A., Kvashnin, A. N., Laurila, T., Lawler, M. J., Mai, H., Makhmutov, V., Mauldin III, R. L., Molteni, U., Nichman, L., Nie, W., Ojdanic, A., Onnela, A., Piel, F., Quéléver, L. L. J., Rissanen, M. P., Sarnela, N., Schallhart, S., Sengupta, K., Simon, M., Stolzenburg, D., Stozhkov, Y., Tröstl, J., Viisanen, Y., Vogel, A. L., Wagner, A. C., Xiao, M., Ye, P., Baltensperger, U., Curtius, J., Donahue, N. M., Flagan, R. C., Gallagher, M., Hansel, A., Smith, J. N., Tomé, A., Winkler, P. M., Worsnop, D., Ehn, M., Sipilä, M., Kerminen, V.-M., Petäjä, T., and Kulmala, M.: The role of ions in new particle formation in the CLOUD chamber, Atmos. Chem. Phys., 17, 15181–15197, https://doi.org/10.5194/acp-17-15181-2017, 2017.

Werle, P., Slemr, F., Maurer, K., Kormann, R., Mücke, R., and Jänker, B.: Near-and mid-infrared laser-optical sensors for gas analysis, Opt. Laser. Eng., 37, 101–114, 2002.

WHO: Ambient air pollution: A global assessment of exposure and burden of disease, WHO Press, Geneva, Switzerland, 2016.

Wildt, J., Mentel, T. F., Kiendler-Scharr, A., Hoffmann, T., Andres, S., Ehn, M., Kleist, E., Müsgen, P., Rohrer, F., Rudich, Y., Springer, M., Tillmann, R., and Wahner, A.: Suppression of new particle formation from monoterpene oxidation by NO_x, Atmos. Chem. Phys., 14, 2789–2804, https://doi.org/10.5194/acp-14-2789-2014, 2014.

Williamson, C. J., Kupc, A., Axisa, D., Bilsback, K. R., Bui, T., Campuzano-Jost, P., Dollner, M., Froyd, K. D., Hodshire, A. L., Jimenez, J. L., Kodros, J. K., Luo, G., Murphy, D. M., Nault, B. A., Ray, E. A., Weinzierl, B., Wilson, J. C., Yu, F., Yu, P., Pierce, J. R., and Brock, C. A.: A large source of cloud condensation nuclei from new particle formation in the tropics, Nature, 574, 399–403, 2019.

Wimmer, D., Lehtipalo, K., Franchin, A., Kangasluoma, J., Kreissl, F., Kürten, A., Kupc, A., Metzger, A., Mikkilä, J., Petäjä, T., Riccobono, F., Vanhanen, J., Kulmala, M., and Curtius, J.: Performance of diethylene glycol-based particle counters in the sub-3 nm size range, Atmos. Meas. Tech., 6, 1793–1804, https://doi.org/10.5194/amt-6-1793-2013, 2013.

Wimmer, D., Lehtipalo, K., Nieminen, T., Duplissy, J., Ehrhart, S., Almeida, J., Rondo, L., Franchin, A., Kreissl, F., Bianchi, F., Manninen, H. E., Kulmala, M., Curtius, J., and Petäjä, T.: Technical Note: Using DEG-CPCs at upper tropospheric temperatures, Atmos. Chem. Phys., 15, 7547–7555, https://doi.org/10.5194/acp-15-7547-2015, 2015.

Ye, P., Zhao, Y., Chuang, W. K., Robinson, A. L., and Donahue, N. M.: Secondary organic aerosol production from pinanediol, a semi-volatile surrogate for first-generation oxidation products of monoterpenes, Atmos. Chem. Phys., 18, 6171–6186, https://doi.org/10.5194/acp-18-6171-2018, 2018.

Ye, Q., Wang, M., Hofbauer, V., Stolzenburg, D., Chen, D., Schervish, M., Vogel, A. L., Mauldin, R. L., Baalbaki, R., Brilke, S., Dada, L., Dias, A., Duplissy, J., El Haddad, I., Finkenzeller, H., Fischer, L., He, X., Kim, C., Kürten, A., Lamkaddam, H., Lee, C. P., Lehtipalo, K., Leiminger, M., Manninen, H. E., Marten, R., Mentler, B., Partoll, E., Petäjä, T., Rissanen, M. P., Schobesberger, S., Schuchmann, S., Simon, M., Tham, Y. J., Vazquez-Pufleau, M., Wagner, A. C., Wang, Y., Wu, Y., Xiao, M., Baltensperger, U., Curtius, J., Flagan, R., Kirkby, j., Kulmala, M., Volkamer, R., Winkler, P. M., Worsnop, D. R., and Donahue, N. M.: Molecular Composition and Volatility of Nucleated Particles from α-Pinene Oxidation between $-50\,^{\circ}$C and $+25\,^{\circ}$C, Environ. Sci. Technol., 53, 12357–12365, https://doi.org/10.1021/acs.est.9b03265, 2019.

Ziemann, P. J. and Atkinson, R.: Kinetics, products, and mechanisms of secondary organic aerosol formation, Chem. Soc. Rev., 41, 6582–6605, 2012.

Supplement of Atmos. Chem. Phys., 20, 9183–9207, 2020
https://doi.org/10.5194/acp-20-9183-2020-supplement
© Author(s) 2020. This work is distributed under
the Creative Commons Attribution 4.0 License.

Atmospheric Chemistry and Physics
Open Access
EGU

Supplement of

Molecular understanding of new-particle formation from α-pinene between -50 and $+25\,^{\circ}\mathrm{C}$

Mario Simon et al.

Correspondence to: Mario Simon (simon@iau.uni-frankfurt.de) and Joachim Curtius (curtius@iau.uni-frankfurt.de)

The copyright of individual parts of the supplement might differ from the CC BY 4.0 License.

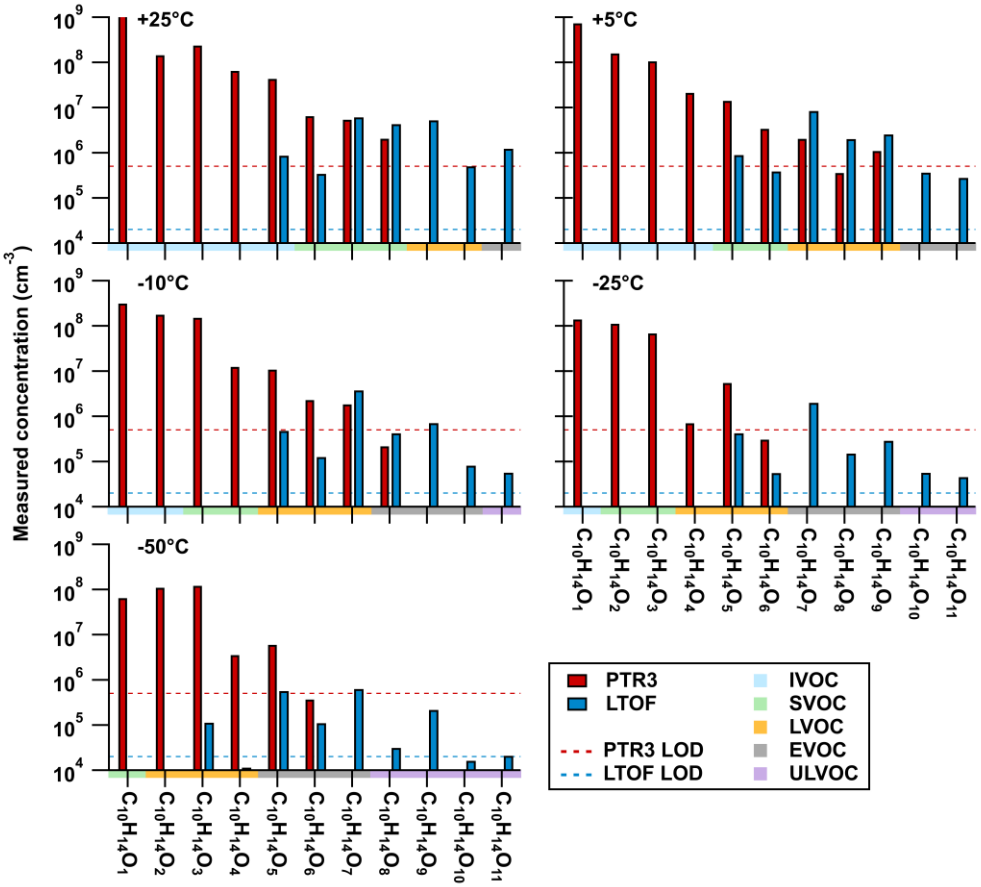
+25°C
+5°C
-10°C
-25°C
-50°C
Measured concentration (cm^{-3})
10^9
10^8
10^7
10^6
10^5
10^4
$C_{10}H_{14}O_1$
$C_{10}H_{14}O_2$
$C_{10}H_{14}O_3$
$C_{10}H_{14}O_4$
$C_{10}H_{14}O_5$
$C_{10}H_{14}O_6$
$C_{10}H_{14}O_7$
$C_{10}H_{14}O_8$
$C_{10}H_{14}O_9$
$C_{10}H_{14}O_{10}$
$C_{10}H_{14}O_{11}$
PTR3
LTOF
PTR3 LOD
LTOF LOD
IVOC
SVOC
LVOC
EVOC
ULVOC

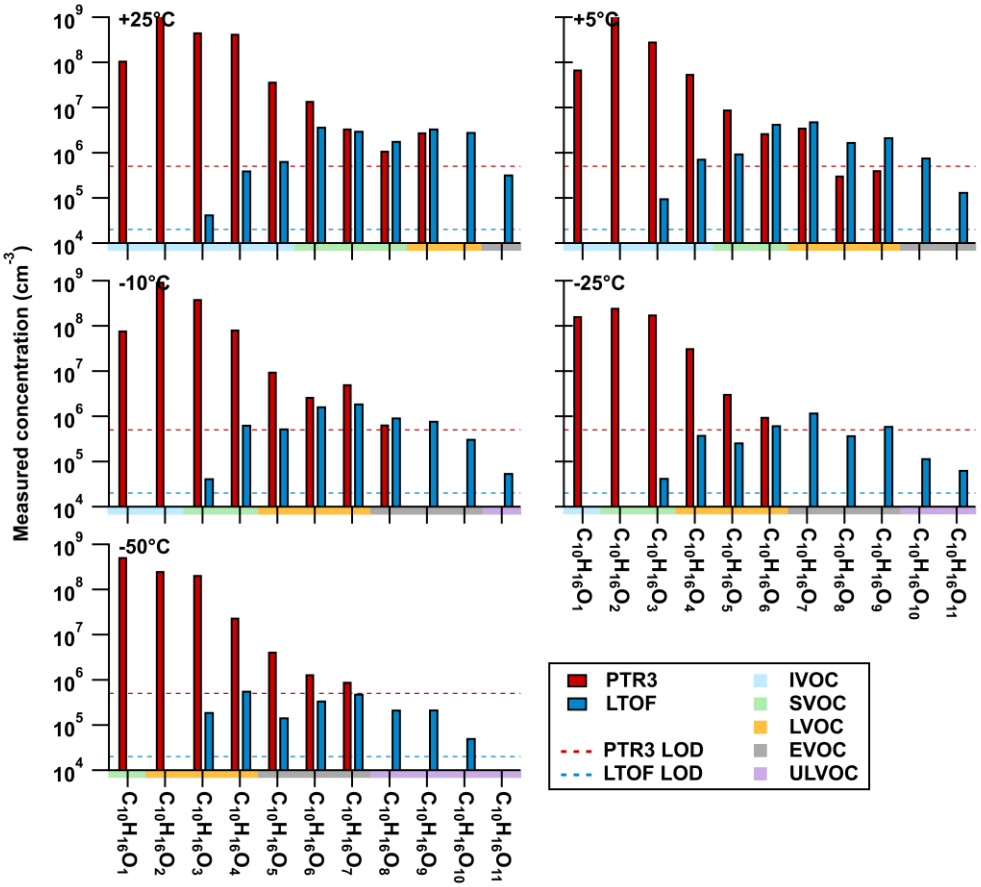

Figure S1*:* Distribution of α-pinene oxidation products at different temperatures.

Quantitative comparison of α-pinene oxidation products measured by the PTR3 instrument (red) and the nitrate CI-APi-TOF (blue) at similar α-pinene oxidation rates. The dashed lines indicate the instrumental LOD for each instrument. The shading of the bottom axes illustrates the corresponding volatility class for each molecule at the given temperature. The PTR3 instrument is capable to measure the lower oxidation states of the oxidation products, while the nitrate CI-APi-TOF is quantitative within the range of higher oxidation states. Both instruments show a good correlation in the O/C range of 0.6 to 0.7. Due to the intense drop in volatility with temperature even low oxidized products are able to nucleate and the PTR3 instrument needs to be included to represent a qualitative evaluation of the nucleating material.

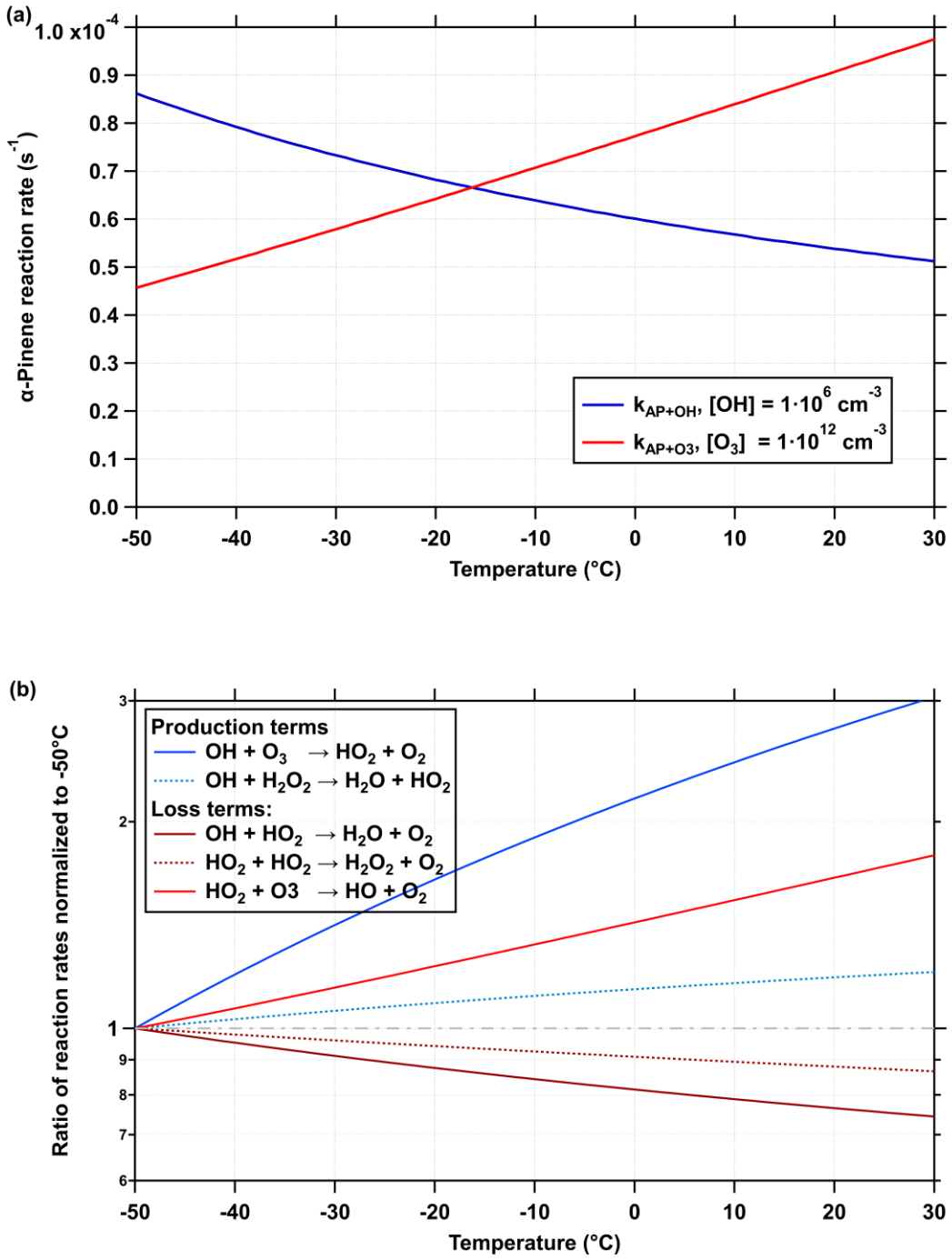

Figure S2: Reaction rate of the α-pinene ozonolysis and OH• oxidation and normalized reaction rates of HO_2• as function of different temperatures.

(a) The temperature dependence of the α-pinene ozonolysis rate (red curve) at typical O_3 mixing ratios of 40 ppb_v compared to the oxidation rate by OH• radicals (blue curve) at typical experimental [OH•]~1e6 cm^{-3}. The OH• oxidation rate is reciprocal with temperature and results in around twice the rate of the ozonolysis at -50 °C for the given experimental concentrations. This ratio is almost reversed for experiments at 25 °C. (b) Temperature dependence of the main

production (green) and loss (red) terms of $HO_2^\bullet$ reaction in the CLOUD chamber normalized to the reaction rate at -50 °C. Both production terms show an increase with increasing in temperature, while only one loss term show a positive and the rest a negative temperature dependence. This will result in sum to a higher mean $HO_2^\bullet$ concentration at higher temperatures.

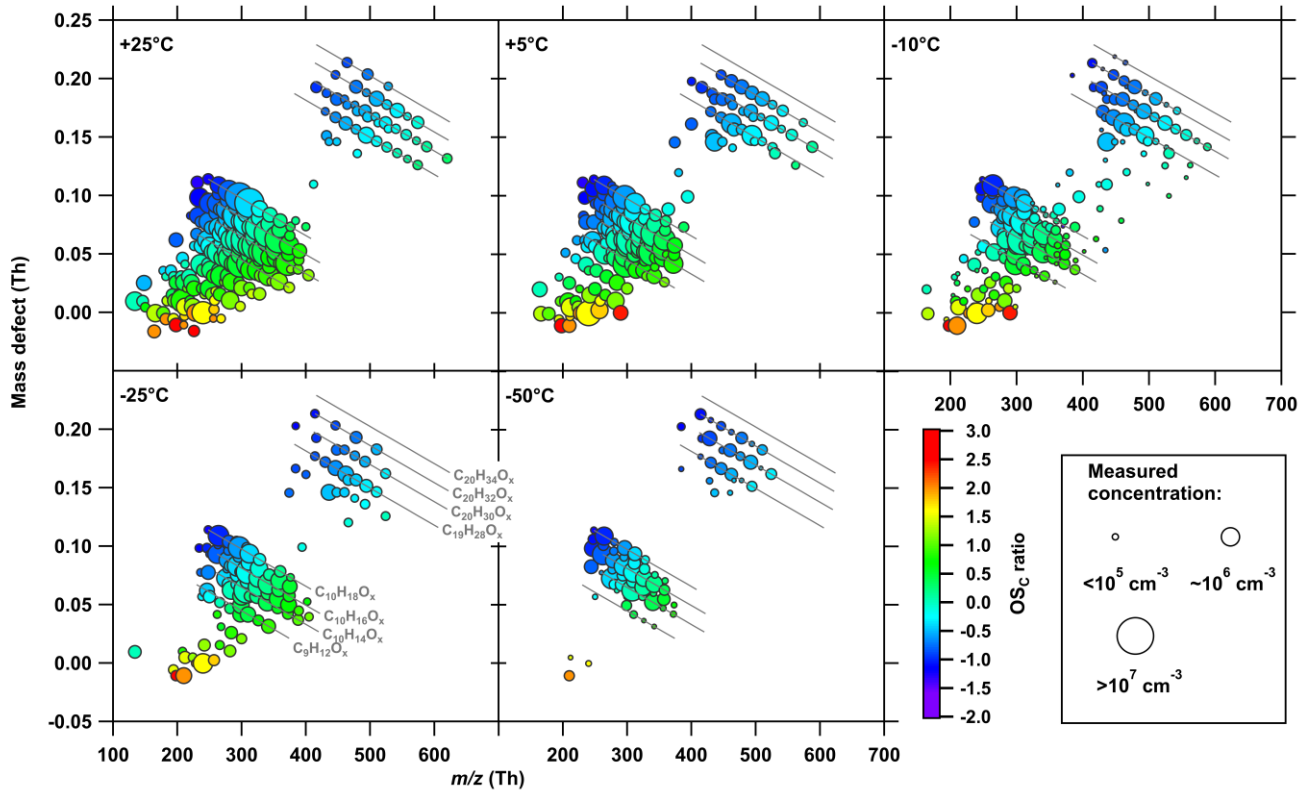

Figure S3: Illustration of the oxidation states of the HOMs based on their mass-defect at five different temperatures.

The experimental data is consistent to the Figures shown in the main text. For every temperature an approximately similar oxidation rates ($2 - 3 \cdot 10^6$ molecule $\cdot$ cm^{-3} $\cdot$ s^{-1}) is used. The data represent an average of a constant steady-state concentration of about one hour. The color-coding shows the oxidation state of carbon (OS_C) of each individual detected molecule.

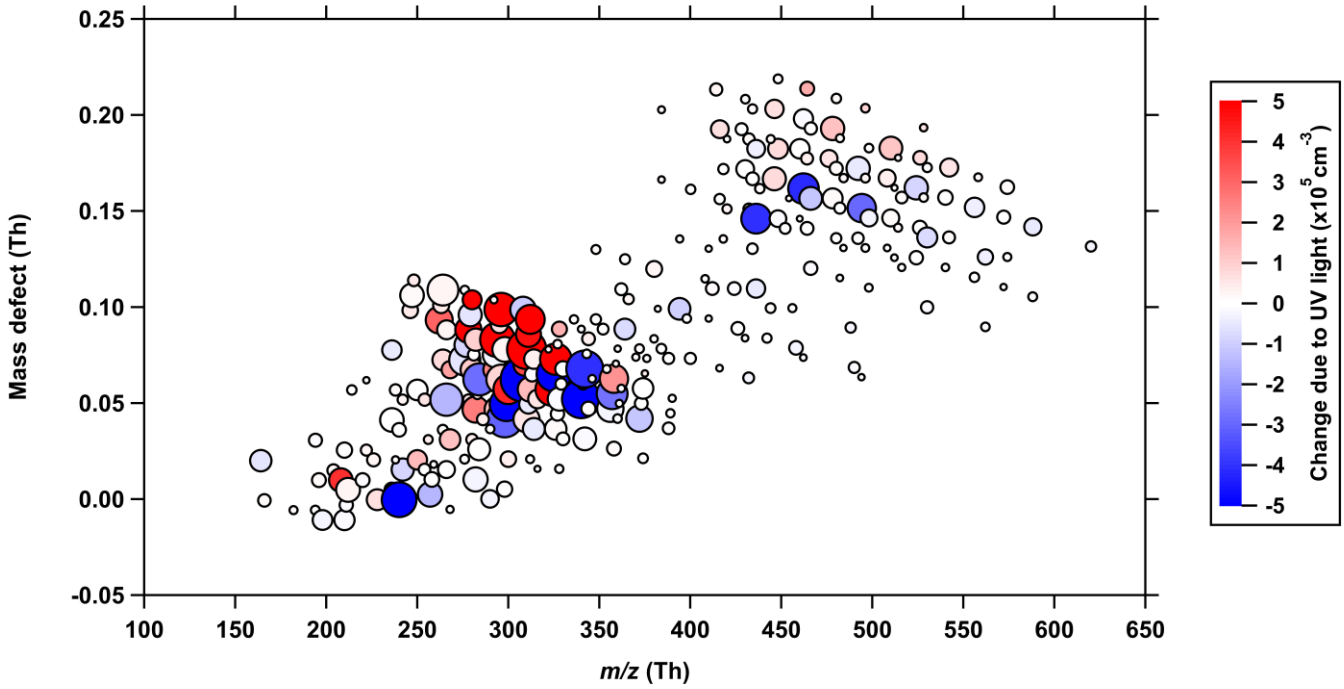

Figure S4: Mass-defect plot of the concentration change of the neutral highly-oxygenated molecules (HOMs) detected by the CI-APi-TOF between dark an UV-illuminated conditions.

The α-pinene and ozone flow into the chamber was kept constant during these runs to allow for a direct comparison. The measured concentration of α-pinene dropped from 618 to 504 pptv, respectively, due to the additional reaction with the elevated $OH^{\bullet}$ radical concentration produced by the UV light. The ozone concentration showed a slight increase from 46 to 48 ppbv. The area of the marker points is logarithmically scaled to their concentration at dark conditions. The color code indicates the change in the intensity of each individual molecule by switching to UV light conditions.

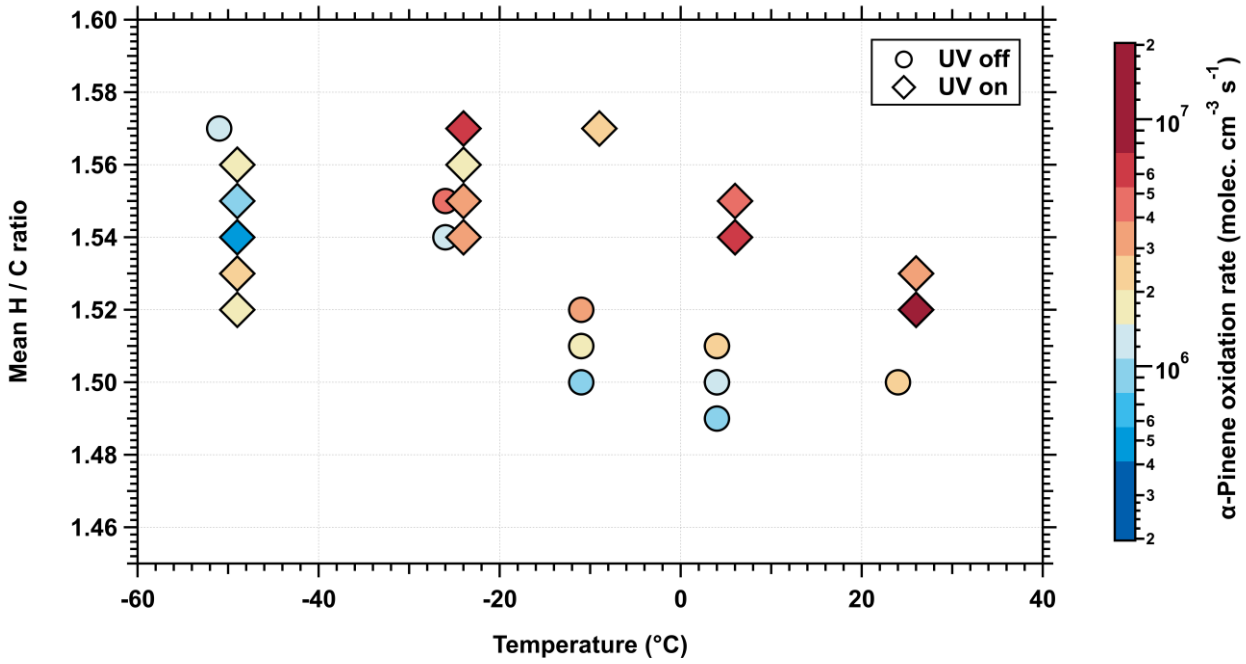

Figure S5: Mean hydrogen-to-carbon (H/C) atomic ratio observed with the CI-APi-TOF for varying α-pinene reacted concentrations for dark (circle) and UV illuminated (diamond) conditions at different temperatures.

The mean H/C at UV illuminated conditions is elevated due to the increased reaction of α-pinene with $OH^{\bullet}$ radicals compared to dark conditions.

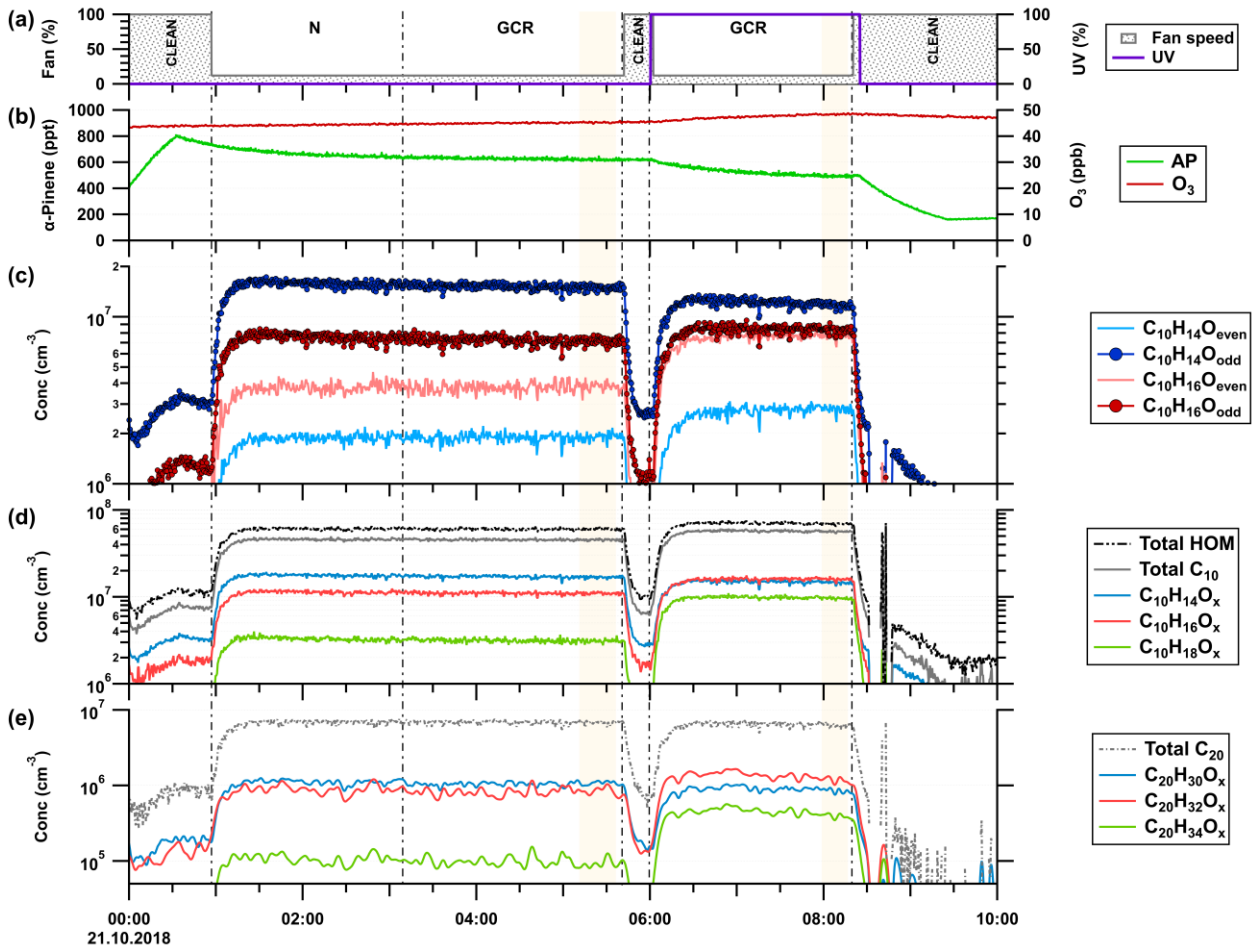

Figure S6: Change of HOM class distribution during an α-pinene oxidation experiment due to UV-illumination.

The α-pinene flow into the chamber was set to a constant level at 00:30 until 8:25am, while the ozone flow was kept constant all the time to ensure a direct comparison during dark and UV illuminated conditions. While there is no change in the HOM distribution when changing from neutral to GCR conditions there is a clear change when the UV light is switched on. The UV light elevates the $OH^{\bullet}$ radical concentration inside the chamber by a factor of 2. Due to the additional oxidation reagents, the α-pinene level drops from 618 to 504 ppt, while the ozone level increases slightly. This also affects the oxidation chemistry. The termination of the $RO_2^{\bullet}$ radicals by $HO_x^{\bullet}$ radicals is increased which leads to more $C_{10}H_{14,16}O_{even}$ products. Also, the initial oxidation reaction by $OH^{\bullet}$ radical addition will form more carbon-centered radicals with the formula $C_{10}H_{17}O_x^{\bullet}$. These radicals lead to closed-shell products with 16 and 18 hydrogen atoms in the monomer molecule as well as 32 and 34 hydrogen atoms in the dimer products (blue and green trace in the lower panels). The increase of the $C_{10}H_{18}O_x$ closed-shell products by a factor of 3.5 also concludes an increase of $OH^{\bullet}$ radicals by a factor of 2 as the products are square root

dependent on the $OH^{\bullet}$ radical concentration. The higher $HO_x^{\bullet}$ radical concentration also change the $RO_2^{\bullet}$ radical termination pathway. Due to the competition with the $RO_2^{\bullet}+RO_2^{\bullet}$ termination which forms the extremely low volatile C_{20}-dimers this additional pathway will end up in more C_{10}-monomer molecules while the total amount of HOMs are slightly elevated.